UNIVERSITY OF OKLAHOMA GRADUATE COLLEGE

ANALYSIS OF THE AERODYNAMIC PERFORMANCE OF CARBON FIBER WINGS FABRICATED USING 3D PRINTED MOLDS WITH VARIED SURFACE FINISHES

A THESIS

SUBMITTED TO THE GRADUATE FACULTY

In partial fulfillment of the requirements for the

Degree of

MASTER OF SCIENCE

By

ANDY TAN

Norman, Oklahoma

2025

Downloaded from SHAREOK. Persistent Handle URL: https://hdl.handle.net/11244/341212

ANALYSIS OF THE AERODYNAMIC PERFORMANCE OF CARBON FIBER WINGS FABRICATED USING 3D PRINTED MOLDS WITH VARIED SURFACE FINISHES

A THESIS APPROVED FOR THE

SCHOOL OF AEROSPACE AND MECHANICAL ENGINEERING

BY THE COMMITTEE CONSISTING OF

Dr. Yingtao Liu, Chair

Dr. Jivtesh Garg

Dr. Wei Sun

© Copyright by Andy Tan 2025

All Rights Reserved.

Acknowledgements

I first want to thank Dr. Yingtao Liu for his unwavering support throughout the past year as my advisor. He has consistently shown patience, kindness, and a genuine desire to help. No matter the circumstance, he has always reminded me that he is here for me and will do whatever he can to help me reach my goals. For that, I cannot thank him enough. I would also like to thank Dr. Wei Sun and Dr. Jivtesh Garg for serving on my thesis committee and for supporting me throughout this process.

I would also like to thank the friends I've made throughout my years studying engineering at OU. Whether through classes, the Sooner Racing Team, or research, I've been fortunate to meet people who have truly shaped my college experience. I've spent countless long days and late nights working on engineering projects, and I'm fortunate to have had friends by my side who made the work fun and helped me grow as an engineer.

Lastly, I want to thank my family for making any of this possible. My mom and dad came to America without knowing any English and have worked tirelessly—always putting my sisters and me first—to give us the opportunities we have today. While I'm proud to have fulfilled my own ambitions, I'm even prouder to show my parents that their hard work and sacrifices were worth it.

Table of Contents

Chapter 1: Introduction 1

1.1 Uses and Manufacturing Methods of Carbon Fiber Reinforced Polymers 1

1.2 Additive Manufacturing of Molds 3

1.3 Impact of 3D Printed Mold Roughness on CFRP Surface Finish 4

1.4 Literature Review: Surface Roughness of FDM Printed Parts 6

1.5 Literature Review: Effect of Surface Roughness on Aerodynamics 9

1.6 Thesis Overview 11

Chapter 2: Manufacture of Molds and CFRP 12

2.1 CFRP Wing Skin Fabrication Overview 12

2.2 3D Printer and Filament Selection 12

2.3 Mold Design 19

2.4 Print Settings 23

2.5 Surface Preparation 28

2.6 Layup Process 32

Chapter 3: Surface Roughness Testing 42

3.1 Surface Roughness Tester 42

3.2 Measurement Procedure 43

3.3 Roughness Measurements of Molds 45

3.4 Roughness Measurements of Wing Skins 50

3.5 Mold and Wing Skin Roughness Comparison 52

Chapter 4: CFD Simulations 54

4.1 Simulation Setup 54

4.2 CFD Results: Coefficient of Lift and Drag 60

4.3 CFD Results: Boundary Layer Analysis 64

Chapter 5: Conclusions and Future Work 69

5.1 Summary of Findings 69

5.2 Mold Surface Roughness Targets 70

5.3 Mold Print Parameters and Surface Finishing 71

5.4 Future Work 72

References 74

List of Figures

Figure 1: Experimental Process Parameters [33] 8
Figure 2: Process Parameter Impact on Print Time [33] 8
Figure 3: Creality Ender 3 V2 [38] 12
Figure 4: NACA 2412 Airfoil [47] 19
Figure 5: CAD Model of the NACA 2412 Airfoil Mold 19
Figure 6: Compressive Specific Strength of Infill Patterns [50] 20
Figure 7: Gauge Pressure of Vacuum Bag 21
Figure 8: FEA Stress Analysis of Wing Skin Mold 22
Figure 9: FEA Deformation Analysis of Wing Skin Mold 22
Figure 10: Print Orientation of Mold 23
Figure 11: Print Time at Various Infill % 25
Figure 12: Material Usage vs Print Time 26
Figure 13: Layer Height vs Print Time 27
Figure 14: Printed Wing Skin Mold 28
Figure 15: (Left) Unsanded Mold (Right) Completely Sanded Mold 30
Figure 16: (Left) Unsanded Coated Mold (Right) Completely Sanded Coated Mold 31
Figure 17: Mold Coated with PVA 34
Figure 18: Saturated Carbon Fiber Sheets During Layup 38
Figure 19: (Left) Peel Ply (Right) Breather Cloth 39
Figure 20: Layup and Vacuum Setup 40
Figure 21: Wing Skins from (a) Base Mold (b) Sanded Mold (c) Coated Mold 41
Figure 22: Surface Roughness Tester [58] 42
Figure 23: Wing Skin Roughness Tester Stand 44

Figure 24: Average Ra of Multiple Sanding Grit Levels 46
Figure 25: Average Rz at Multiple Sanding Grit Levels 46
Figure 26: Average RSm at Multiple Sanding Grit Levels 47
Figure 27: Average Ra of Pre and Post Coating 48
Figure 28: Average Rz of Pre and Post Coating 48
Figure 29: Average RSm of Pre and Post Coating 49
Figure 30: Average Ra of Each Wing Skin 50
Figure 31: Average Rz of Wing Skins 51
Figure 32: Average RSm of Wing Skins 51
Figure 33: CAD Model of Wing for CFD 54
Figure 34: CFD Fluid Volume 55
Figure 35: CFD Mesh 59
Figure 36: CL vs AOA at Re 300,000 61
Figure 37: CL vs AOA at Re 3,100,000 61
Figure 38: CL vs AOA at Re 5,400,000 62
Figure 39: CD vs AOA at Re 300,000 63
Figure 40: CD vs AOA at Re 3,100,000 63
Figure 41: CD vs AOA at Re 5,400,000 64
Figure 42: Turbulent Kinetic Energy Contour of Ra 0 μm Wing 65
Figure 43: Turbulent Kinetic Energy Contour of Ra 6.529 μm Wing 65
Figure 44: TKE Contour of Ra 0 μm Wing at Re 300,000 and AOA 18° 66
Figure 45: TKE Contour of Ra 1.951 μm Wing at Re 300,000 and AOA 18° 67
Figure 46: TKE Contour of Ra 0 μm wing at Re 300,000 and 6° AOA 68
Figure 47: TKE Contour of Ra 6.529 μm wing at Re 300,000 and 6° AOA 68

List of Tables

Table 1: Mechanical Properties of PLA, ABS, and PETG.....13

Table 2: Coefficient of Thermal Expansion of Thermoplastics 14

Table 3: Softening Temperatures of Thermoplastic Filaments 17

Table 4: Surface Roughness Parameters..... 43

Table 5: Base Mold Surface Roughness Parameters 45

Table 6: Surface Roughness Comparison of Finished Molds 49

Table 7: Mold and Wing Skin Surface Roughness Parameters..... 52

Table 8: Boundary Conditions of Fluid Volume..... 56

Table 9: Boundary Layer Meshing Parameters..... 59

Table 10: Converted Ra to Sand Grain Roughness 60

Abstract

This thesis investigates the aerodynamic impact of surface roughness in carbon fiber reinforced polymer (CFRP) wing skins fabricated using 3D-printed molds. Additive manufacturing via fused deposition modeling (FDM) offers a low-cost method for producing custom molds but often introduces surface imperfections that transfer to the final CFRP part. Mold surface quality is critical for airfoils, where roughness can alter boundary layer behavior.

Three mold surface conditions—unsanded, sanded, and coated—were used to produce CFRP wing skins with varying roughness. Surface roughness was measured using a stylus profilometer and quantified through Ra, Rz, and RSm. Wing skins were fabricated using a wet layup process with vacuum bagging at room temperature. Wing skin roughness was then measured to assess fidelity to the mold.

Using these values, computational fluid dynamics (CFD) simulations in ANSYS Fluent evaluated aerodynamic performance at Reynolds numbers of 300,000, 3,100,000, and 5,400,000. Higher surface roughness caused earlier boundary layer transition, increased drag, and reduced lift. The coated mold produced the smoothest surface and best aerodynamic results.

This study shows that FDM induced surface roughness affects aerodynamic efficiency and emphasizes the value of post-processing in performance-sensitive, low-cost composite manufacturing.

Chapter 1: Introduction

1.1 Uses and Manufacturing Methods of Carbon Fiber Reinforced Polymers

Over the past half-century, carbon fiber reinforced polymers (CFRP) have been increasingly adopted as an alternative to traditional materials [1]. Among its many advantages, CFRP stands out for its notably higher strength-to-weight ratio compared to commonly used materials. CFRP's specific strength varies by type but is typically significantly higher than that of aluminum and steel, making it especially valuable in weight-sensitive applications [2-4]. Examples of this include the Boeing 787 Dreamliner, Formula 1 cars, and wind turbine blades, all of which see performance benefits from CFRP. The Boeing 787 Dreamliner is constructed using 50% CFRP by weight, making it the primary material for the fuselage and wings. This extensive use of CFRP significantly reduces the aircraft's weight, leading to lower fuel consumption and reduced operational costs [5]. Formula 1 cars are predominantly constructed from CFRP to minimize weight, as any excess mass reduces cornering speed, impairs acceleration and braking, which ultimately compromises lap times [6]. For wind turbines, the combination of high strength and low weight allows for longer blades while remaining lightweight to produce as much power as possible [7]. Beyond these major sectors, CFRP also sees use in prosthetics, boat hulls, and high-performance sporting equipment [8-10]. As CFRP use has become more commonplace, its advantages have become accessible even to students, particularly in collegiate engineering competitions. Teams in events such as Formula SAE (FSAE) and AIAA Design-Build-Fly (DBF) employ CFRP in much the same way as industrial applications, although on a smaller scale [11-12].

With the expanding range of CFRP applications, numerous manufacturing methods have been developed, each offering distinct advantages and disadvantages suited to specific needs. The basic process of manufacturing CFRP involves applying a polymer—typically an epoxy resin—to layers of carbon fiber laid onto a mold and then cured. Common methods for manufacturing CFRP are wet layups, vacuum assisted resin transfer molding (VARTM), resin transfer molding (RTM), prepreg layups, and filament winding. In wet layups, resin is manually applied to dry carbon fiber layers. VARTM involves sealing dry fiber in a vacuum bag where the resin is drawn in using the vacuum to saturate the fibers. RTM is similar to VARTM but uses pressurized resin injected into a closed mold. Prepreg layups use carbon fiber sheets that are already saturated with partially cured resin. Filament winding is where carbon fiber tows are pulled through resin and then wound around a rotating mandrel. Determined by the layup method, curing can be done at room temperature, at a high temperature in an oven or at a high temperature and pressure in an autoclave [13].

The selected layup and curing method dictate the requirements for the mold itself. For example, molds used in autoclaves must withstand elevated pressures and temperatures, as well as match the thermal expansion properties of carbon fiber. For mass production, molds must be durable enough for repeated use [14]. Materials commonly used for molds are fiberglass, aluminum, steel, CFRP, and various high-density foams. Each material has its advantages suited for certain applications but can be expensive, require large amounts of machining and labor to produce [15]. For mass production in large industries, this is permissible but for low production or rapid prototyping where the mold doesn't have to meet such stringent requirements a cheaper and more accessible mold type is desired.

1.2 Additive Manufacturing of Molds

Additive manufacturing (AM), commonly referred to as 3D printing, offers a viable alternative for producing CFRP molds [16]. Unlike traditional subtractive methods, which involve cutting away material to shape a part, AM builds components layer by layer, offering greater design flexibility and reduced material waste. There exist many types of AM, distinguished by how the material is added. The most commonly known and accessible method is fused deposition modeling (FDM) where a heated thermoplastic filament is extruded from a nozzle onto a print bed. As each printed layer cools and solidifies, a new one is added, stacking to create the final model. Thermoplastics such as polylactic acid (PLA), acrylonitrile butadiene styrene (ABS) and polyethylene terephthalate glycol-modified (PETG) are widely used with FDM printing as they are cheap and easy to print [17].

FDM printing offers several advantages that make it particularly well-suited for CFRP mold production, especially when compared to conventional mold-making techniques. Unlike CNC machining, which requires significant labor and material waste, FDM enables quick and cost-effective fabrication with minimal setup. This allows for rapid iteration of mold designs, reducing both lead times and prototyping costs [18]. Additionally, FDM's ability to produce complex geometries enables the creation of custom mold features that would be challenging to machine using conventional methods [19]. These advantages make FDM a practical solution in cases where machining facilities for metal or foam molds are unavailable, production volumes are low, and rapid prototyping is needed. Additionally, FDM is an ideal alternative when the cost of conventional molds is impractical and when temperature and strength demands are relatively low.

Despite its advantages, FDM printing presents material limitations that impact mold capabilities and, consequently, the CFRP layup methods available. Standard thermoplastics such as PLA, ABS, and PETG have low strength and soften at relatively low temperatures, making them unsuitable for molds used in autoclaves and ovens [20]. However, for CFRP layups that cure at room or low temperatures—where an autoclave or oven is unavailable, unnecessary, or cost-prohibitive—FDM-printed molds remain a practical alternative. Polyether ether ketone (PEEK) exhibits superior strength and heat resistance compared to PLA, ABS, and PETG, making it well-suited for autoclave applications [21]. However, its high-cost limits practicality, particularly in applications where cost-effectiveness is a primary concern.

1.3 Impact of 3D Printed Mold Roughness on CFRP Surface Finish

The surface quality of a mold directly influences the final surface finish of the CFRP component produced from it [22]. In traditional manufacturing, molds are typically made from machined aluminum, steel, or polished composite materials, ensuring a smooth, defect-free surface that minimizes irregularities in the final CFRP part [23]. However, additively manufactured molds, particularly those fabricated using FDM, inherently possess surface imperfections due to the nature of the layer-by-layer extrusion process [24]. These imperfections will transfer onto the CFRP surface, noticeably affecting the surface roughness and visual appearance.

Since aerodynamic surfaces are commonly manufactured from CFRP, the surface roughness of a 3D-printed mold can significantly impact the aerodynamic performance of the final component. Surface roughness influences airflow behavior, particularly by disrupting the boundary layer, the thin region of air that forms near a surface due to

viscous effects as the body moves through air. Within this layer, air velocity transitions from zero at the surface (due to the no-slip condition) to the freestream velocity at some distance away. The boundary layer can exist in different states, each with distinct aerodynamic consequences. A laminar boundary layer is characterized by smooth, orderly airflow with minimal mixing, resulting in lower skin friction drag. However, it is more susceptible to flow separation, which can reduce efficiency. In contrast, a turbulent boundary layer contains irregular, high-mixing airflow, leading to higher skin friction drag but greater resistance to flow separation [25]. Along the length of a surface, a laminar boundary layer naturally transitions to a turbulent state, but surface roughness can cause premature transition. This early transition can lead to higher drag and, in some cases, boundary layer separation, where the airflow detaches from the surface, resulting in increased drag and reduced lift—both undesirable effects in aerodynamic applications [26]. These factors highlight the importance of minimizing surface roughness in CFRP components to maintain optimal aerodynamic performance.

The roughness of FDM-printed molds is influenced by several key print settings, including layer height, print speed, nozzle diameter, and print orientation. Layer height has the most significant impact—thicker layers create more pronounced layer lines, while thinner layers result in a smoother surface at the cost of increased print time. Print speed also affects roughness, as improper settings can cause inconsistencies in layer adhesion, leading to uneven textures or surface gaps. Nozzle diameter influences resolution, with smaller nozzles producing finer details but extending print duration [27]. Print orientation further determines surface quality, as printing parallel to the mold's surface

minimizes layer lines, whereas vertical surfaces tend to develop more pronounced ridges [28].

To improve surface finish, various post-processing techniques can be applied. Sanding and polishing physically smooth the surface but are labor-intensive. Epoxy or other coatings can be used to help fill in layer lines, reducing roughness [29]. While these methods enhance mold quality, they can also significantly increase print time or require extensive manual labor. To optimize the balance between surface roughness, print time, and post-processing effort, it is essential to characterize the impact of mold roughness on the aerodynamic performance of CFRP parts. This analysis will help establish an acceptable surface finish standard for FDM-printed molds and identify the most efficient methods to achieve it.

1.4 Literature Review: Surface Roughness of FDM Printed Parts

The effect of print settings and parameters on the surface roughness of FDM components is a topic that has been widely studied. In a study conducted at the University of Vigo in Spain, researchers attempted to develop a model to predict the surface roughness of 3D printed components based on the print settings used. They varied the layer thickness, inclination, rotation about the z-axis, and radius of curvature of three different part types. The part types include: one with a flat face, one with a concave face, and one with a convex face. All samples were printed with the same nozzle temperature, envelope temperature, and material (ABS). Every sample's surface roughness was measured using a Taylor-surf measurement device to obtain values of average roughness (Ra). Using Ra values the Signal-to-noise ratio (S/N) was calculated and compared between print setting variations for each part. The magnitudes of S/N vary between each

part for the same print setting and the % change differs as well but the overall trends of which settings result in lower/higher surface roughness are the same between all three parts. They found that a lower layer thickness, higher inclination, higher radius, and having the part oriented along the X or Y-axis led to a lower S/N / roughness. They also conducted an Analysis of Variance analysis (ANOVA) to determine which print setting contributed the most to surface roughness. In order from biggest to smallest contribution they are inclination, layer thickness, curve radius, and z-axis rotation [30].

A similar study conducted by researchers at the Kalinga Institute of Industrial Technology in India varied the layer thickness, inclination, raster width and overlap distance and measured the resulting surface roughness. They found that increasing layer thickness had by far the biggest impact on increasing surface roughness. Inclination, raster width, and overlap distance all had a much lower effect. An increase in overlap distance, inclination, and decrease in raster width decreased surface roughness [31].

In another published paper, layer thickness was once again found to be a big contributor to surface roughness. It was also found that as infill density increases, the surface roughness decreases but the effect isn't as pronounced as decreasing the layer thickness [32].

While the previous papers evaluated the impact of the major printing parameters, a paper from the Technical University of Liberec in the Czech Republic analyzed the

effects of 17 processes parameters, many of which are not commonly modified, and can be found in the figure below.

Nozzle temperature
Retrieval length
Retrieval speed
Layer height
Width of the extruded line
Number of walls
Thickness of the top layer
Fill shape
Fill print speed
Wall print speed
Print speed of top layers
Crossing speed
Support shape
Quantity of extruded material
Orientation of the part on the base
Percentage of fill
The shape of the top layer filler

Figure 1: Experimental Process Parameters [33]

All these parameters were varied on a 3-level scale and the resulting printed parts were measured for surface roughness. The most impactful parameters on surface roughness were identified along with the influence of each print setting on print time.

Parameter	Part percentage / %	Cumulative frequency / %
Layer height	37.41	37.41
Wall print speed	14.35	51.76
Top later print speed	13.65	65.41
Print fill speed	12.94	78.35
Number of walls	4.24	82.59
Fill percent	3.29	85.88
Top layer thickness	3.06	88.94
Width of extruded line	2.82	91.76
Shape of top layer	2.35	94.12
Extruded materials possibilities	2.12	96.24
Shape supported	1.41	97.65
Orientation of the part at the base	1.18	98.82
Fill shape	1.18	100

Figure 2: Process Parameter Impact on Print Time [33]

Some of the most influential print settings on surface roughness such as layer height and print speeds also have a big effect on print speed while shape, infill pattern, and part orientation were found to have a big impact on surface roughness while not affecting print time as much [33]. The ability to reduce surface roughness without

drastically increasing print time makes shape, infill pattern and print orientation key parameters to optimize if possible.

The differences in surface roughness between filaments has also been studied. In a paper published by Istanbul technical University in Turkey, researchers printed samples made from PLA, PETG, and ABS. For each filament, they printed samples at three different layer heights of 0.2mm, 0.3mm, and 0.4mm and measured the Ra of each one. Across every measurement they consistently found that the samples printed from PLA had a lower roughness than the samples made of PETG and ABS with PETG having the second lowest roughness. The gaps in roughness between each filament is so large that even though reducing layer height has been repeatedly found to have a big effect on surface roughness, the 0.4mm layer height of the smoother filaments are still smoother than the 0.2mm of the rougher filaments [34].

Across multiple studies, the effect of several FDM process parameters on the surface roughness of parts has been consistently documented. While the magnitudes vary from study to study, the relation from parameter to parameter is largely similar. Layer thickness and print inclination are regularly found to be the biggest influences on surface roughness. While the effect of printing parameters on the surface roughness of FDM parts is well studied, quantification of the effectiveness of post processing techniques is not. Manual smoothing, application of filler material, and chemical smoothing are all known to be effective but to what extent is not well documented [35-36].

1.5 Literature Review: Effect of Surface Roughness on Aerodynamics

The effect of surface roughness on the performance of aerodynamic bodies is one that is also widely studied. In a paper published by researchers from Beihang University in

China, they looked at the effects of surface roughness on the boundary layer formation and resulting losses of a 2d turbine blade cascade. They conducted their experiments using CFX for their computational fluid dynamics (CFD) simulations. They used three different roughness sizes (K_s) of 26μm, 53μm, and 110μm. These simulations were also conducted at four different Reynolds numbers (Re) of 60000, 157000, 250000, and 300000. It was found that the high-pressure side of the airfoil was barely affected by surface roughness so the results were focused on the low-pressure side. The conclusions drawn from the simulations consisted of analyzing the coefficient of friction (C_f) and shape factor along the surface of the airfoil. When the C_f drops to zero the boundary layer starts to separate, and a negative C_f indicates a separated boundary layer. Shape factor provides similar observations as it increases with boundary layer thickness growth and increases by a large amount when the boundary layer is separated.

When looking at the pressure loss downstream of the cascade, at a Re of 157000 the peak value of loss decreases as roughness increases. This is due to the increased roughness reducing the size of the separation bubble. However, at a Re of 250000 the 110μm roughness level has the most loss while 26μm and 53μm still have less loss than the perfectly smooth airfoil. At a Re of 300000 every level of roughness is worse than the perfectly smooth surface. The change from some amount of roughness being advantageous in reducing pressure losses to being consistently harmful is attributed to the decrease in boundary layer thickness as the Re increases. As the boundary layer thickness sufficiently approaches the height of the thickness level, the interactions between the two become more substantial, resulting in an increasingly early transition to a separated boundary layer [37].

1.6 Thesis Overview

This thesis investigates how surface roughness in CFRP wing skins, fabricated using 3D-printed molds, influences key aerodynamic traits, including the coefficient of lift (C_L) and coefficient of drag (C_D). By varying the mold's surface finish, the resulting wing skin roughness will be measured and incorporated into CFD simulations to evaluate aerodynamic performance. These results, along with manufacturing considerations, will inform the optimal mold surface roughness. Chapter 2 details the mold and wing skin production process. Chapter 3 covers roughness testing of the molds and wing skins. Chapter 4 discusses the CFD simulation setup and results. Chapter 5 concludes the study with recommendations on optimal mold surface roughness, printing and post-processing methods, and potential future work.

Chapter 2: Manufacture of Molds and CFRP

2.1 CFRP Wing Skin Fabrication Overview

The objective of the sample production was to create multiple 3D-printed molds with varying levels of post-process surface finishing. The resulting CFRP wing skins exhibited different roughness levels based on these variations. Rather than aiming for the smoothest possible mold or a specific target roughness, the goal was to establish a range of achievable roughness levels using common methods such as sanding or surface coatings. These roughness levels served as baseline inputs for CFD simulations. Based on the CFD results, the ideal combination of print parameters and surface finishing were determined. As a result, some of the initial sample production methods were not optimized for a specific roughness target but instead focused on generating a representative range of surface conditions.

2.2 3D Printer and Filament Selection

To produce the molds for the CFRP layup process a Creality Ender 3 V2 was used. This widely used entry-level FDM printer can print the molds required for this study.



Figure 3: Creality Ender 3 V2 [38]

The Ender 3 V2 features a 220 x 220 x 250 mm build volume with a 0.4 mm nozzle. It supports nozzle temperatures up to 260°C and a heated bed temperature of 100°C, enabling it to print common thermoplastics such as PLA, ABS, and PETG, which were considered for use for the molds [38]. To maintain simplicity, the printer was used in its stock configuration without modifications.

When selecting the filament for the molds, the key considerations were strength, print accuracy, heat resistance, and chemical smoothing. Factors such as cost, print temperature, moisture absorption, UV resistance, chemical resistance (except for compatibility with the laminating resin), and print bed adhesion were deemed either similar across all three filaments, irrelevant to this study, or both [39-41].

The molds were used for wet layups and cured in ambient temperature under a vacuum. This meant the molds were subjected to a force over an extended period. For the filaments to be viable they must have sufficient strength to withstand vacuum bag without failure. The Young's modulus and tensile strength of PLA, ABS, and PETG can be found below.

Table 1: Mechanical Properties of PLA, ABS, and PETG

Material	Young's Modulus (X-Y) (MPa)	Tensile Strength (X-Y) (MPa)	Tensile Strength (Z) (MPa)
PLA [39]	2641 ± 328	47.1 ± 1.2	38.9 ± 0.5
ABS [40]	1685 ± 81	25.1 ± 0.5	21.3 ± 0.6
PETG [41]	1986 ± 268	44.3 ± 1.3	38.9 ± 3.0

In Table 1 the material properties were reported as either X-Y or Z. These specify the plane at which the property applies. X-Y is the horizontal plane which is parallel to the print bed. Z is the vertical direction, or the direction normal to the print bed. PLA has by far the highest Young's Modulus (X-Y) which is a measure of how stiff a material is before plastic deformation occurs. PLA's Young's Modulus is 56.7% higher than that of ABS and 33.0% higher than PETG's. PLA also has the highest tensile strength (X-Y) which is the stress required to cause a material to fail in tension. PLA's tensile strength (X-Y) is 87.6% higher than ABS' and only 6.3% higher than PETG's. PLA and PETG have nearly identical tensile strength (Z) and are 82.6% higher than ABS'. PLA and PETG's higher tensile strength would allow molds printed from them to potentially have a lower infill % than one printed from ABS to achieve the same strength. The PLA and PETG molds could be printed quicker while consuming less material.

The accuracy of the printed mold is also crucial, as it directly affects the shape of the resulting airfoil skin and, consequently, its aerodynamic performance. However, FDM parts are not perfectly precise due to various factors, with shrinkage being a significant one. Shrinkage occurs when the thermoplastic contracts during cooling, leading to dimensional changes that can alter the final part's geometry.

Table 2: Coefficient of Thermal Expansion of Thermoplastics

Thermoplastic	Coefficient of Thermal Expansion (μm/m·°C)
PLA [42]	68
ABS [42]	90
PETG [42]	60

As shown in Table 2, PLA, ABS, and PETG each have different Coefficients of Thermal Expansion (CTE), resulting in varying degrees of shrinkage for molds printed from these materials. PLA and PETG have significantly lower CTE values compared to ABS, meaning that a mold printed from ABS will experience greater shrinkage than one made from PLA or PETG. This difference in thermal expansion must be considered when selecting a filament for mold fabrication to ensure dimensional accuracy.

Studies have analyzed the shrinkage of PLA, ABS, and PETG in the x, y, and z directions of a 3D printer, corresponding to length, width, and height, respectively, and compared their dimensional accuracy at various layer heights. While layer height has not shown a consistent effect on shrinkage, notable differences have been observed in the accuracy of different filaments. Across all three materials, length (x-axis) accuracy is high, exceeding 99%. PETG is the most accurate, with a measured accuracy of 99.99%, while ABS has the lowest at 99.21%. However, when examining width (y-axis) accuracy, discrepancies start to emerge—PLA is the most accurate at 97.72%, whereas ABS lags at 90.94%. A similar trend is observed in height (z-axis) accuracy, where PETG leads at 99.11%, while ABS is the least accurate at 90.68% [34]. Overall, ABS has been consistently found to be the least accurate across width and height by a significant margin, whereas PLA and PETG demonstrate similar accuracy levels across all three dimensions.

The effects of shrinkage can be mitigated by upscaling the model in slicer software, provided that the shrinkage is well understood and accurately accounted for. Additionally, a heated printing environment can help minimize shrinkage by reducing temperature fluctuations and ensuring more uniform cooling. When using ABS, greater consideration is required to achieve accurate molds due to its higher shrinkage rate compared to PLA

and PETG. In contrast, PLA and PETG molds experience significantly less shrinkage, making them easier to work with.

The temperature resistance of the filament is also important because, during CFRP layups, the exothermic reaction of the epoxy resin generates heat that can warp, soften, or degrade the mold material. The mold must be able to withstand this heat without deforming, as any distortion could lead to dimensional inaccuracies in the final part. Additionally, if the mold softens too much, it may collapse under vacuum pressure, compromising both surface quality and structural integrity.

The exothermic temperature generated during curing depends on several factors, including the hardener's cure time (faster cures produce higher temperatures, while slower cures remain cooler), the amount of epoxy resin used (larger volumes generate more heat), the number of carbon fiber layers (thicker laminates retain more heat), and the surface area-to-thickness ratio of the layup (greater surface area allows for better heat dissipation). In some applications, epoxy resin can reach temperatures up to 200°C, depending on these factors [43]. However, for the wing skins produced in this thesis, the slow-curing room-temperature epoxy minimizes heat buildup, the low amount of epoxy resin used reduces overall exotherm, the relatively small number of carbon fiber layers limits heat retention, and the large surface area relative to thickness promotes effective heat dissipation, all of which contributes to a significantly lower exothermic temperature.

Table 3: Softening Temperatures of Thermoplastic Filaments

Thermoplastic	Softening Temperature (˚C)
PLA [39]	64.2
ABS [40]	103.4
PETG [41]	85.1

As shown in Table 3, ABS has the highest softening temperature, followed by PETG, and then PLA. Given the factors that contribute to a lower exothermic temperature in the wing skins produced for this thesis, all three filaments are highly likely to withstand the curing temperatures without compromising mold performance. PLA should endure this specific application, but for cases involving larger volumes of epoxy resin and significantly more layers of carbon fiber, it is unlikely to maintain structural integrity under the increased heat.

Lastly, the last major factor in filament selection for this thesis is the ability to be chemically smoothed. Chemical smoothing allows for high-quality mold surface finishes without requiring extensive manual post-processing or significantly increasing print time. However, the feasibility of this process depends on the type of filament, as some materials are resistant to common solvents or require hazardous chemicals.

PLA is difficult to chemically smooth due to its resistance to common solvents. Ethyl acetate or tetrahydrofuran (THF) can be used but often result in uneven smoothing and surface defects, while their toxicity further limits practicality [44]. ABS is the easiest to smooth, with acetone vapor effectively eliminating layer lines and slightly reinforcing the print. Though flammable and requiring ventilation, acetone remains a safe and

practical option [45]. PETG resists acetone and requires stronger solvents like methyl ethyl ketone (MEK) or dichloromethane (DCM), both of which pose significant health risks. While DCM vapor can smooth PETG, its toxicity makes it impractical, and MEK brushing is inconsistent and weakens the part, making PETG unsuitable for chemical smoothing [46].

While PLA and PETG require hazardous chemicals that yield inconsistent results, ABS can be chemically smoothed easily and effectively with minimal effort. ABS is by far the best filament to be chemically smoothed.

In conclusion, PETG is the optimal choice for the molds due to its superior balance of strength, dimensional accuracy, and heat resistance. While ABS has the highest temperature resistance among the three filaments and is the only one truly viable for chemical smoothing, its significantly higher shrinkage and lower tensile strength increase the risk of dimensional inaccuracies both during printing and under vacuum pressure during curing. Although ABS' ability to be smoothed with acetone is a distinct advantage, this thesis will later explore an alternative post processing method that requires a comparable amount of work to achieve the same surface finish. PLA, despite its high stiffness and excellent dimensional accuracy, may lack sufficient heat resistance for some use cases. Thus, PETG is the most suitable filament for the applications of this thesis.

2.3 Mold Design

The CFRP wing skins produced for surface roughness testing were based on the NACA 2412 airfoil. It is shown in the figure below.

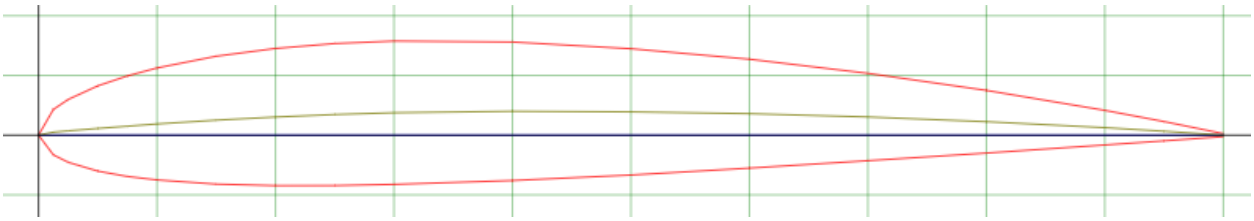


Figure 4: NACA 2412 Airfoil [47]

This airfoil was selected due to its widespread use across various applications. The NACA 2412 is employed in everything from unmanned aerial vehicles to small aircraft like the Cessna 172 [48-49]. Its broad range of applications exposes it to a wide spectrum of Reynolds numbers, which this thesis aims to simulate. By doing so, this study assessed the effects of surface roughness under multiple real-world conditions. The mold was designed using SolidWorks CAD and can be seen below.

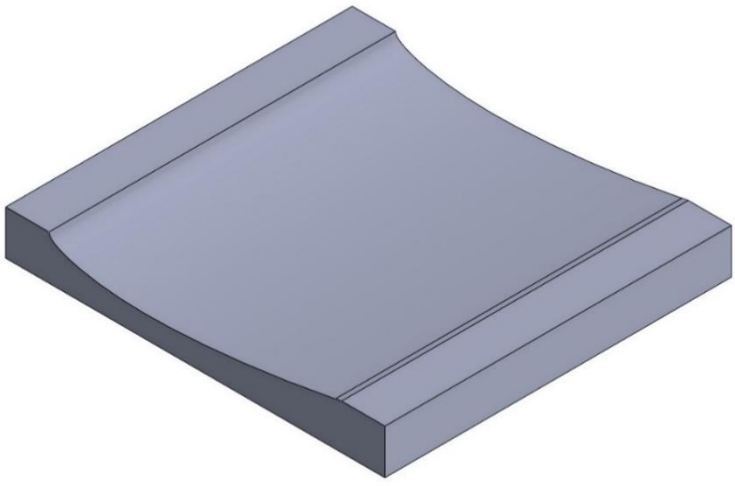


Figure 5: CAD Model of the NACA 2412 Airfoil Mold

Since the effects of surface roughness on the aerodynamics of the high-pressure side of the airfoil are minimal, only the mold for the low-pressure side was produced [37].

The surface roughness measurements of the low-pressure side mold and wing skin are assumed to be similar to the high-pressure side, allowing for an approximation of equivalence. The mold's dimensions were constrained by the Ender 3 V2 print bed size, limiting the size of the wing skins. Regardless, the produced wing skins were sufficient for surface roughness testing. The design maintains a constant chord as incorporating twist or a taper would complicate the mold without offering additional benefits for roughness measurements. To facilitate manufacturing, flat sections were added at the leading and trailing edges, providing extra surface area for laying carbon fiber. These sections were later trimmed to create a uniform, clean edge. Additionally, extra material was added to the bottom of the mold to enhance strength and reduce the risk of breakage under vacuum pressure or during manual surface smoothing.

To enhance the strength of the mold, the strongest infill pattern was chosen. Since infill patterns have not been shown to significantly impact the surface roughness of FDM parts, the selection was based on specific strength and print time as the primary determining factors [33].

Infill Pattern	Average α
Cross	2531.92
Grid	2505.04
Triangles	2392.60
Concentric	2335.80
Tri-hexagonal	2310.20
Lines	2303.82
Cross 3D	2286.24
Zigzag	2207.22
Octet	2117.22
Concentric 3D	2108.83
Cubic	2022.91
Tetrahedral	2004.01
Gyroid	1986.82
Quarter Cubic	1943.71

Figure 6: Compressive Specific Strength of Infill Patterns [50]

As shown in Figure 6, Cross and Grid exhibit the highest average compressive specific strengths across various infill densities. The detailed justifications for choosing Grid over Cross will be further discussed in the Print Settings section but, in short, Grid provides comparable specific strength to Cross while offering a shorter print time.

After completing the CAD design and selecting the infill pattern, the mold was analyzed using ANSYS Finite Element Analysis (FEA) to verify its ability to withstand the pressure inside a vacuum bag.

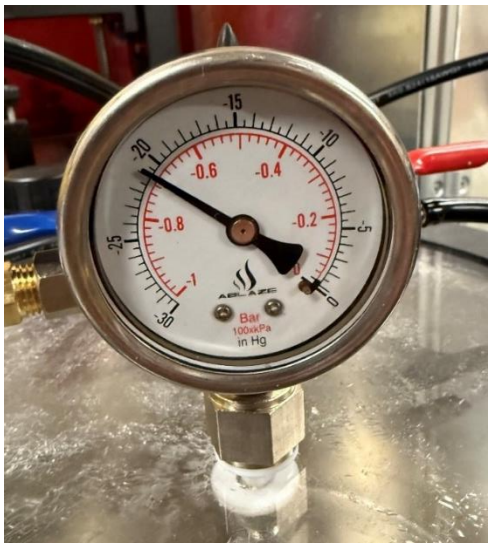


Figure 7: Gauge Pressure of Vacuum Bag

As shown in Figure 7, the gauge pressure inside of the test vacuum bag was roughly -0.7 Bar, or -70 kPa. This pressure was applied as a load in the FEA simulation to analyze the stresses on the 3D-printed mold.

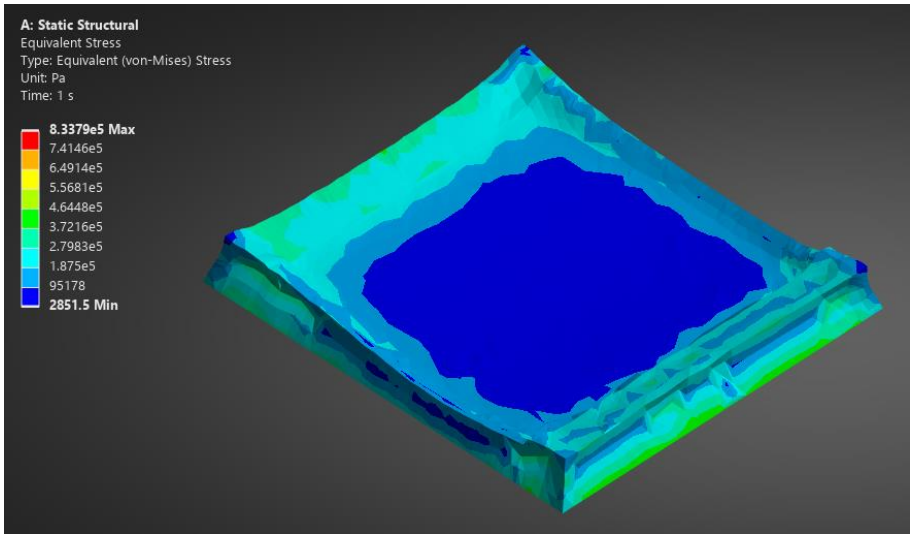


Figure 8: FEA Stress Analysis of Wing Skin Mold

Figure 8 presents the FEA results for a mold with a 10% infill. The simulation shows that the stress induced by the vacuum bag is minimal, with a maximum value of 833,790 Pa. This stress level remains well below the material's ultimate strength, ensuring that the mold can withstand the pressure differential between atmospheric pressure and vacuum pressure without failure. To check for any potential geometric inaccuracies in the carbon wing skin, the deformation of the mold was also measured in the simulation.

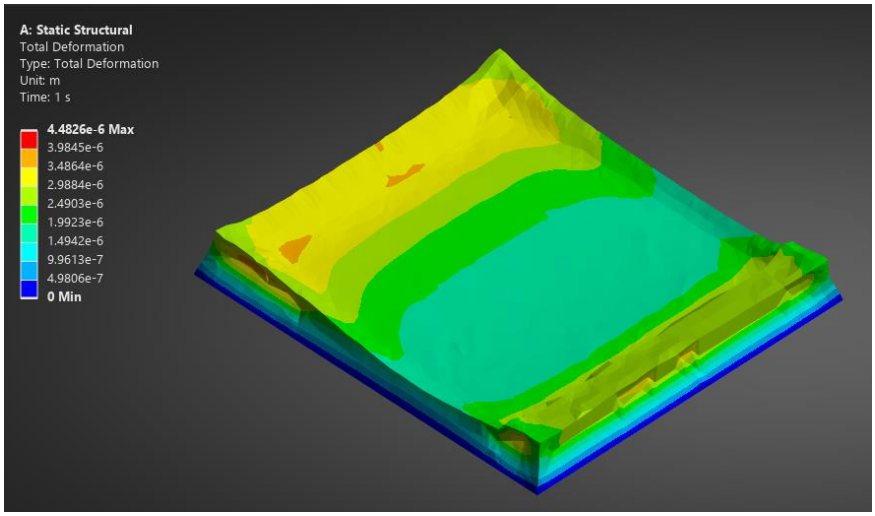


Figure 9: FEA Deformation Analysis of Wing Skin Mold

Figure 9 illustrates the mold deformation under vacuum pressure. With a peak displacement of 4.4825×10^{-6} m, the deformation is negligible, ensuring that the wing skins maintain high geometric accuracy to the true airfoil shape.

2.4 Print Settings

With the wing skin mold design finalized, the next step was to determine the appropriate printer settings for slicing and fabrication. As previously discussed, the goal of the initial samples was to produce a range of representative surface roughness levels commonly achievable with standard 3D printing methods. Print settings were initially selected based on existing research, prioritizing strength or print time when surface roughness was not significantly impacted. For parameters known to influence surface roughness, commonly used or standard settings served as baselines. Once the CFD analysis identified an optimal roughness level, print settings and post-processing techniques were revisited to refine the final surface characteristics.

All of the slicing was done with UltiMaker Cura. To start, the first print parameter to choose was the print orientation of the mold.

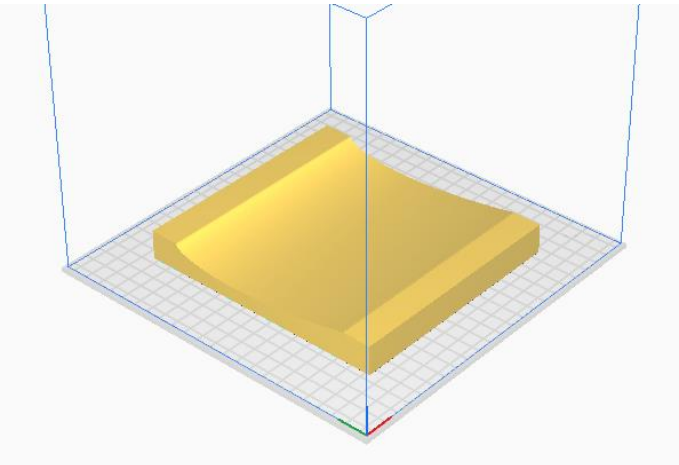


Figure 10: Print Orientation of Mold

The mold was aligned with the X and Y axes, as this orientation has been shown to minimize surface roughness while optimizing the use of the available build volume. It was also positioned flat against the print bed, eliminating the need for supports, which reduced material consumption, print time, and surface roughness caused by inclined printing [30]. Although the mold could have been printed on its symmetrical flat side instead of the underside to further reduce roughness on the airfoil surface, the horizontal orientation was chosen to better reflect the capabilities of industrial large-format FDM printers, which typically have greater X/Y dimensions than Z-height [51-52].

The following print settings primarily influenced the strength of the mold. Any potential impact on surface roughness was likely negligible, making the trade-off in mold strength for a slightly smoother surface unjustifiable. The wall line count was increased from two to three, increasing the wall thickness by 50% and further enhancing structural strength. Additionally, the increased wall thickness provided more material on the outer surfaces, allowing for sanding without drastically reducing the outer wall strength. As previously discussed in the Mold Design section, Cross and Grid infill patterns exhibited the highest specific compressive strength among those available in Cura. However, Grid was chosen over Cross as it had a similar specific compressive strength while requiring shorter print time.

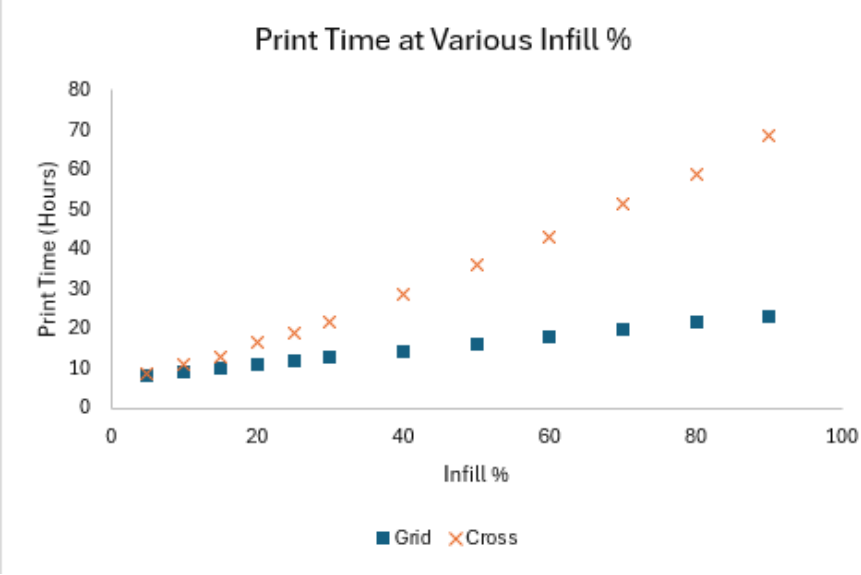


Figure 11: Print Time at Various Infill %

Figure 11 illustrates the impact of varying the infill percentage (%) for Cross and Grid patterns on the required print time. All print times are from a print speed of 70 mm/s. As the infill % increases, the print time for the Grid pattern follows a steady linear trend, whereas the Cross pattern exhibits an exponential increase in print time. At any given infill %, the Grid pattern prints faster than the Cross pattern. However, the material consumption at each infill % differs, leading to variations in compressive strength. As previously shown in Figure 6, both Cross and Grid exhibit similar specific strengths. Therefore, a more accurate comparison of strength relative to print time can be made by evaluating the print time per unit of material used.

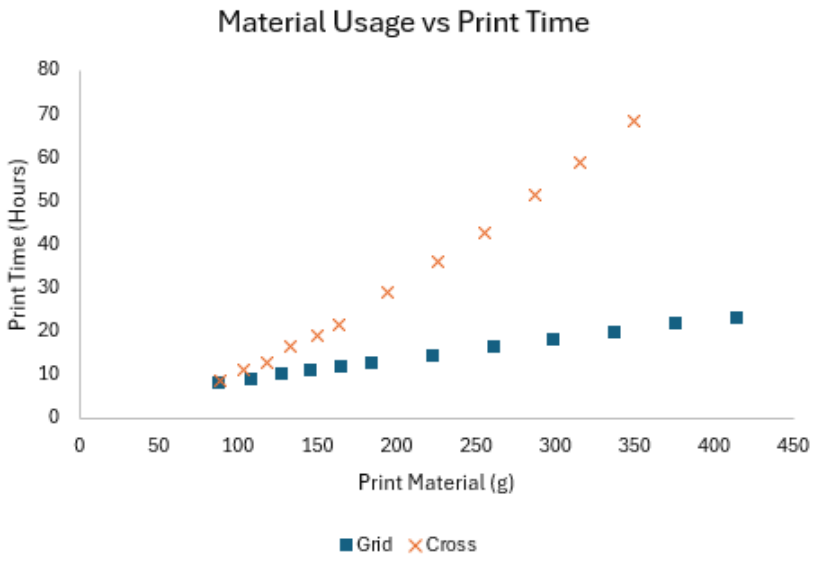


Figure 12: Material Usage vs Print Time

Similar to the comparison of infill % to print time, Grid prints faster than Cross for every given mass of material used. The relationship between print material and print time follows the same trend: Grid exhibits a steady linear increase, whereas Cross follows an exponential growth pattern. This suggests that for any desired level of compressive strength, the Grid infill will always be the faster option to print. For the purposes of this thesis, at an infill percentage of 10%—corresponding to approximately 106 grams of printed material—the difference in print time between the two infill patterns is relatively small compared to higher infill percentages or greater material usage. However, there is still a 19.6% increase in print time from Grid to Cross, highlighting a notable difference in efficiency even at lower infill levels.

Research consistently shows that layer height is the most influential print parameter affecting the surface roughness of FDM parts [30-34]. While reducing layer

height significantly enhances surface smoothness, it also substantially increases print time.

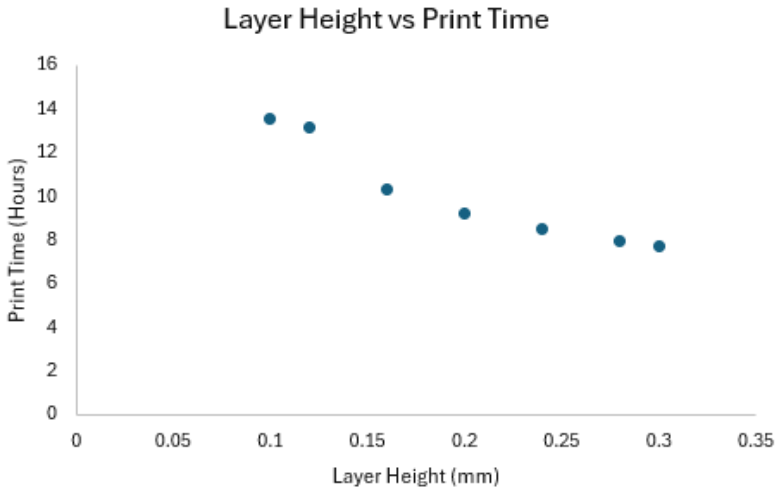


Figure 13: Layer Height vs Print Time

Figure 13 supports the trend that decreasing layer height increases the required print time. In Cura, the default layer height for standard quality is 0.2mm, while the recommended minimum layer height is 0.1mm. Reducing the layer height from 0.2mm to 0.1mm results in a 47.54% increase in print time. For a small part like the wing skin mold, this translates to an additional 4.5 hours of printing. However, for larger parts, the impact is significantly greater, leading to a substantial increase in overall print time. For the molds used in this study, the standard quality layer height (0.2mm) will be applied. However, when reevaluating print parameters based on a target surface roughness, layer height will be the primary parameter adjusted to achieve the desired surface finish.

For other parameters, such as nozzle temperature, build plate temperature, and other print settings, the default values from Cura or the average recommended values from the filament manufacturer were used, as deviations beyond these standard values would not significantly impact mold performance. Combining all of the determined print settings results in the mold shown in the following image.

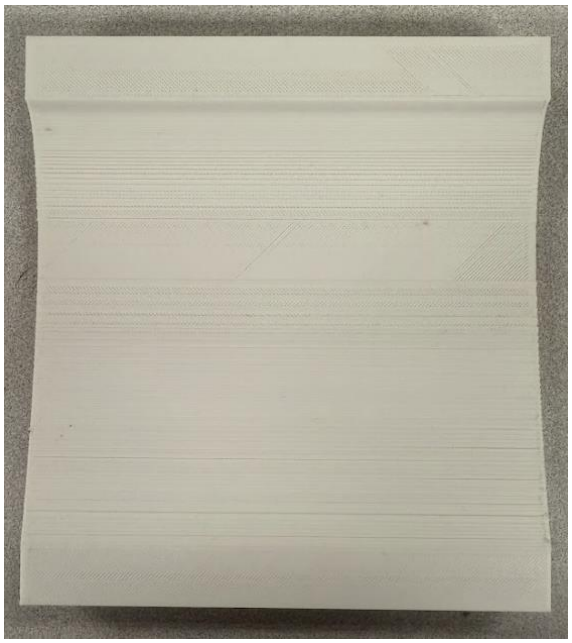


Figure 14: Printed Wing Skin Mold

The layer lines and ridges were readily apparent from looking at the mold's surface. This was not an issue however, as this mold served as the base mold for all the surface treatments aimed at smoothing the surface to achieve varying surface qualities of carbon fiber.

2.5 Surface Preparation

With a standardized 3D-printed mold, the next step was to apply commonly used surface finishing methods to achieve varying levels of mold smoothness. The methods chosen were sanding and applying a filler material. Sanding is an effective but time-

consuming way to smooth out layer lines and reduce roughness, while the filler material method involves filling in the gaps between the layer lines with material and performing light polishing to create a high-quality surface finish. Chemical smoothing was not pursued due to the toxicity and hazards associated with the chemicals required for PETG. To evaluate the effectiveness of these methods, a wing skin will also be made using a mold with no post-processing for a baseline comparison. Additionally, the surface roughness of each mold at every stage of surface finishing was measured to track progress.

Sanding the mold was carried out in stages using progressively finer grits of sandpaper: 180, 320, 500, 1000, and 1500. As the grit increased in fineness, the sanding time required was drastically reduced. Hand sanding with 180 grit took a significant amount of time to remove the initial layer lines, while sanding with 1500 grit required only a couple of minutes to sand the surface. Even with a mold of this small size, the effort required for the rougher grits was significant, highlighting the potential need for orbital sanders or other sanding tools for larger molds. For each stage, the sanding was considered complete when material was no longer being removed, and no visible or tactile differences could be perceived. The following images show the mold before the sanding process and after it was completed.

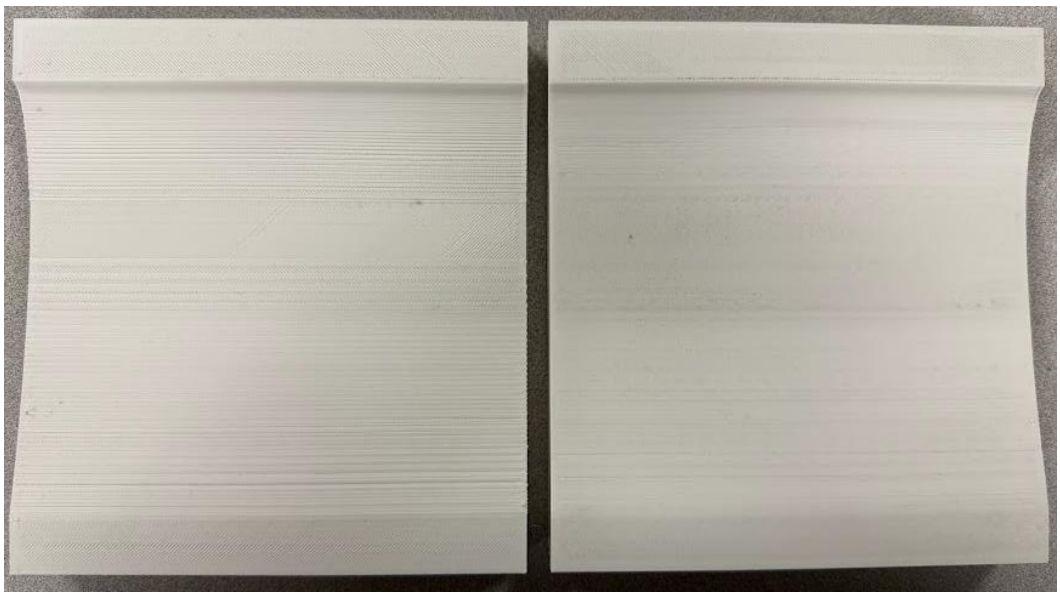


Figure 15: (Left) Unsanded Mold (Right) Completely Sanded Mold

Placing the before-and-after images side by side clearly highlights the differences in layer lines and how they fade with sanding. While the right image in Figure 15 appears noticeably smoother, some deep ridges remain that sanding alone cannot completely remove. This underscores the need for a filler material to achieve a consistently smooth surface.

The other mold post-processing method involved the addition of a filler material. As seen in the sanding process, some layer line ridges were so deep that sanding could not achieve a uniformly smooth surface. To address this, a brush-on-coating was applied to fill in the ridge lines.

The material used was a two-part silicone rubber designed for coating 3D-printed surfaces. This silicone rubber can be sanded and polished, allowing it to achieve a smoothness comparable to a mold sanded to 1500 grit, without retaining occasional deep layer lines. Rather than applying it to a fully sanded mold, it was applied directly to a stock mold. This approach is more efficient, as filling in the layer lines first and then sanding to

a smooth surface requires significantly less time and effort than sanding down the layer lines to achieve smoothness.

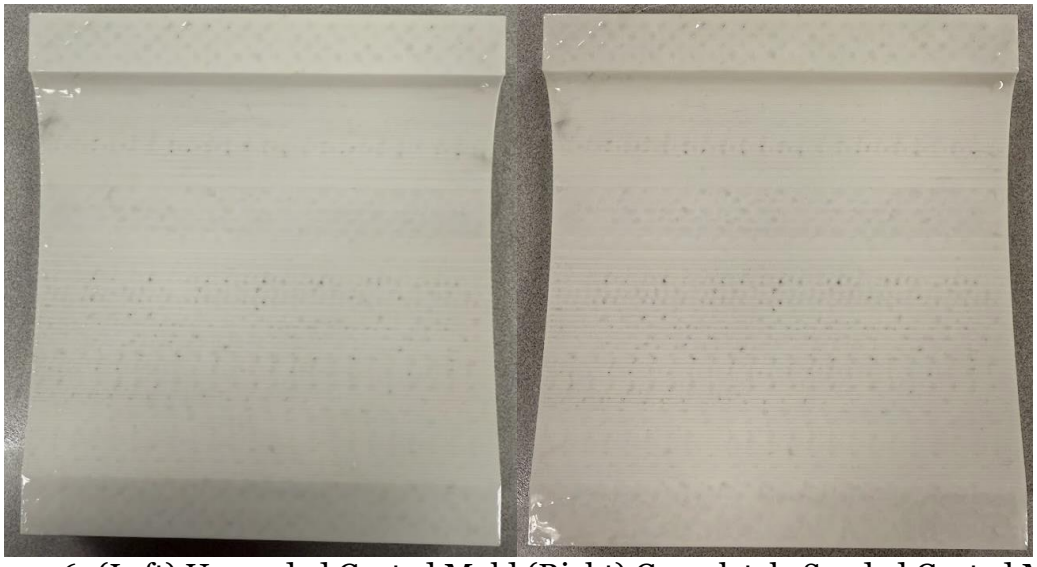


Figure 16: (Left) Unsanded Coated Mold (Right) Completely Sanded Coated Mold

Figure 16 (Left) shows the mold after being coated with silicone rubber, while Figure 16 (Right) displays the coated mold after sanding up to 1500 grit. During the coating process, the amount of material added was kept to a minimum to prevent any alteration to the mold's shape, which could compromise the geometric accuracy of any wing skins produced from it. Once the coating had solidified, the surface felt noticeably smoother, with no detectable layer lines. However, inconsistencies in the coating's application and solidification were apparent, which necessitated the sanding process.

The same sanding process as the previous mold was applied, using grits ranging from 180 to 1500. Sanding was again considered complete when no more material was removed, and no tactile or visual changes were observed. The sanding process for the coated mold was significantly faster than for the bare PETG mold. The silicone rubber was exceptionally easy to sand, reducing the required time to approximately 25% of that

needed for the uncoated mold. This efficiency was further enhanced by the fact that sanding to achieve a smooth surface, rather than directly removing layer lines, requires far less material removal—and consequently, less time. The finished mold benefited greatly from the coating and sanding, as it felt slightly smoother than the 1500-grit sanded bare PETG mold and no longer exhibited occasional deep ridge lines.

With the completion of molds featuring varying surface finishes, the CFRP layup process can now be performed to produce the wing skins.

2.6 Layup Process

Since the purpose of using 3D-printed molds is to provide a low-cost alternative for producing CFRP molds, the selected layup process should align with that objective. In situations where 3D-printed molds are necessary or offer the most benefits—such as in rapid prototyping or low-production applications, the advantages of hand layups complement those of 3D-printed molds. Hand layups are the most affordable CFRP manufacturing method, requiring minimal equipment and setup while avoiding the high costs associated with other processes.

In contrast, prepreg layups, RTM, and VARTM remain expensive, even when paired with low-cost 3D-printed molds. Prepreg layups require costly pre-impregnated carbon fiber sheets, controlled storage conditions, and high-temperature autoclave curing, making them impractical for budget-conscious applications. RTM and VARTM involve more complex infrastructure compared to hand layups, including specialized resin injection systems and rigid, precisely sealed molds capable of withstanding injection pressures. These additional requirements increase both material and equipment costs, making these methods less practical for applications where affordability is a key factor.

Given these considerations, hand layups are the most practical and economical choice, aligning with the cost-saving benefits of 3D-printed molds while still producing functional CFRP components.

A room-temperature hand layup process involves manually applying liquid epoxy resin to layers of dry carbon fiber fabric placed onto a mold. The resin is worked into the fibers using a brush or roller to ensure thorough saturation and bonding between layers. Once the layup is complete, the part is typically enclosed in a vacuum bag to apply uniform pressure, remove excess resin, and eliminate air pockets. The assembly is then left to cure at ambient conditions, with curing time depending on the specific resin system used. This method is simple, cost-effective, and requires minimal equipment, making it ideal for applications using 3D-printed molds.

To begin, layers of polyvinyl alcohol (PVA) were applied to the mold surface. PVA is a water- and alcohol-based release film that forms a barrier between the mold and the resin. It is resistant to the solvents in the epoxy resin used for CFRP, preventing adhesion and allowing the cured carbon fiber to be easily separated from the mold surface without damage.

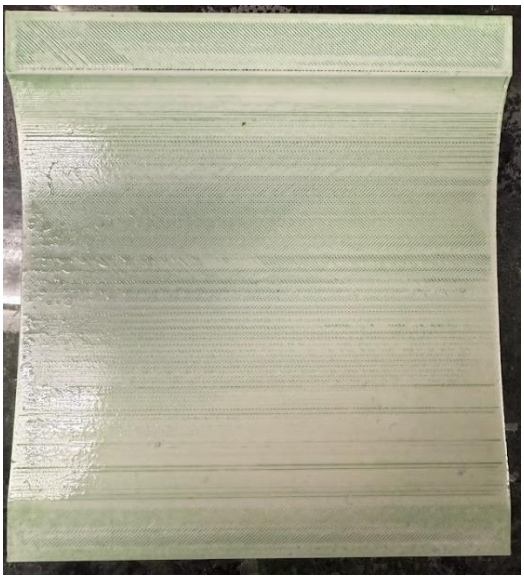


Figure 17: Mold Coated with PVA

PVA was applied to the mold using a roller brush in its liquid form. As it dried upon exposure to air, it formed a thin, solid release layer. Multiple layers were applied sequentially, allowing each to dry before adding the next. After seven layers, the mold developed a distinct green appearance, as shown in Figure 17. Once the PVA application was completed the mold was ready for the wet layup.

The carbon fiber used was 2×2 twill 3k, where 2×2 twill refers to the weave pattern, and 3k indicates that each tow contained 3,000 individual filaments [54]. While the type of carbon fiber used is not expected to impact the resulting surface roughness, the 3k fabric was chosen for its relevance to aerospace and automotive applications, aligning with potential uses. It offers a good balance of strength and weight, making it suitable for structural applications. Additionally, the twill weave's diagonal pattern improved drapability, allowing the fabric to conform to complex mold shapes with minimal distortion.

For each wing skin, three layers of carbon fiber were used. Since the wing skins were intended solely for surface roughness testing, there were no specific strength or thickness requirements. However, three layers were chosen to mitigate the risk of misalignment in a single-ply layup, which could lead to an uneven surface. Additionally, using multiple layers ensured a continuous, uniform carbon wing skin suitable for accurate surface roughness measurements. The fiber orientation followed a 0-degree, 45-degree, and 0-degree alternating pattern. While carbon fiber is an anisotropic material and real applications use varied fiber orientations to provide strength in multiple directions, in this case, the varied orientation was included simply to introduce fiber variation within the layup, not to mimic real-world structural design.

To cut the carbon fiber fabric, 5-inch by 5.5-inch sections were laid out on the roll of carbon fiber, secured with tape, and then cut with scissors. The 5-inch dimension ensured that the carbon did not extend beyond the span of the wing mold, while the 5.5-inch dimension allowed the fabric to follow the full arc length of the wing mold, with extra material extending into the flat runoff areas. Tape was applied not only to mark cut lines but also to prevent the weave from shifting or fraying during cutting. The tape lines served as cut guides, and care was taken to cut as close to the tape edge as possible to ensure minimal tape remained on the carbon fiber sheets used for the layup, reducing the risk of contamination or potential delaminations in the final part. The cuts were strategically placed so that the thin taped edges were positioned in the mold's excess material regions, which were later trimmed away to produce clean edges. For the 45-degree fiber layer, the same cutting method was used, but the fabric square was rotated 45 degrees before taping and cutting.

A thin epoxy resin and 3:1 medium cure hardener was used based on their suitability for achieving high-quality composite layups. The low-viscosity resin allows for ease of wetting of carbon fiber, ensuring thorough impregnation and minimizing void content, which is crucial for structural performance. The medium cure hardener provides a balanced working time, offering a pot life of 20–25 minutes at 80°F and a full cure within 8–10 hours, allowing sufficient time for lay-up while maintaining short manufacturing times [55-56]. This resin-hardener system follows a standard epoxy formulation commonly used in composite fabrication, making it representative of the typical manufacturing experience. Its selection ensures that the results of this study align with general expectations for epoxy-based composites

To determine the ideal amount of epoxy resin for wet layups, a common rule of thumb is the 50/50 fiber-to-resin mass ratio [57]. If too little epoxy resin is applied, the fabric may remain unsaturated in some areas, resulting in weak regions within the final part. Conversely, applying too much epoxy resin adds unnecessary weight and increases material costs without improving structural strength. The process in determining the mass of resin to use is outlined below.

$$\frac{Mass}{Surface\ Area}\ of\ Carbon\ Fiber: 203\frac{g}{m\text{^}2}$$

$$Surface\ Area\ of\ 1\ Sheet: 5in\ x\ 5.5in = 27.5in^2$$

$$27.5in^2 \div 1550\ =\ 0.0177419\ m^2$$

$$203\frac{g}{m^2}\ x\ 0.0177419\ m^2 =\ 3.6016057\frac{g}{Sheet}$$

$$3.6016057\frac{g}{Sheet}\ x\ 3\frac{Sheets}{Wing\ Skin} = \ 10.8048171\frac{g}{Wing\ Skin}$$

$$Safety\ Factor = 1.5$$

$$Mass\ of\ Resin = 1.5\ x\ 10.8048171\frac{g}{Wing\ Skin} = \ 16.20722565\frac{g}{Wing\ Skin}$$

$$Epoxy\ Resin\ to\ Hardener\ Ratio: 3:1$$

$$Mass\ of\ Epoxy\ Resin = \ 16.20722565g\ x\frac{3}{4} = \ 12.1554192375g$$

$$Mass\ of\ Hardener = \ 12.1554192375g\ x\frac{1}{3} = \ 4.0518064125g$$

The required mass of resin was determined based on the mass per unit area of the carbon fiber fabric. Since the size of the carbon fiber sheets for the layup was already established, a simple unit conversion allowed for the calculation of the total resin needed for a three-ply wing skin. To account for potential losses—such as epoxy remaining in the mixing cup, minor misapplications, or other irregularities, a safety factor was applied. Any small excess of epoxy resin was later compressed out of the carbon fiber and absorbed by the breather film. Using the resin-to-hardener ratio, the required mass of each component was calculated. The appropriate amounts were then measured and manually mixed. With the carbon fiber sheets cut and the resin prepared, the layup process could begin.

On the PVA-coated mold, the layup process proceeded as follows. First, a thin layer of epoxy was applied to the mold surface. The first carbon fiber sheet was then placed onto the mold, followed by another application of epoxy, which was spread evenly using a squeegee. This process was repeated for each subsequent layer until all carbon fiber sheets were laid and fully saturated with epoxy. The end of this stage can be shown in Figure 18.

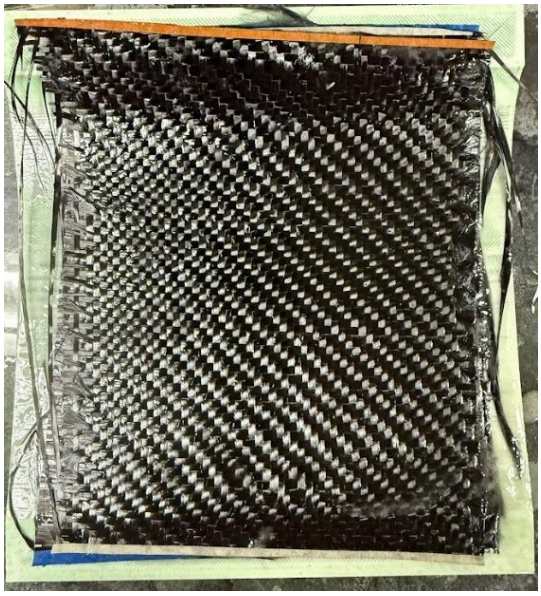


Figure 18: Saturated Carbon Fiber Sheets During Layup

Following this, a layer of peel ply was placed over the saturated carbon fiber sheets. Peel ply is a removable fabric that prevents direct bonding between the carbon fiber and subsequent layers. Its primary purpose in this layup was to allow the breather cloth to be placed on top without sticking to the carbon fiber. Additionally, peel ply imparts a matte surface finish to the cured carbon.

Breather cloth, placed over the peel ply, acts as a permeable layer that maintains airflow within the vacuum bag. It does not fully compress under vacuum pressure, allowing trapped air to be evacuated while also absorbing any excess epoxy squeezed out

of the carbon fiber during the vacuum process. These two steps can be seen in the figures below.

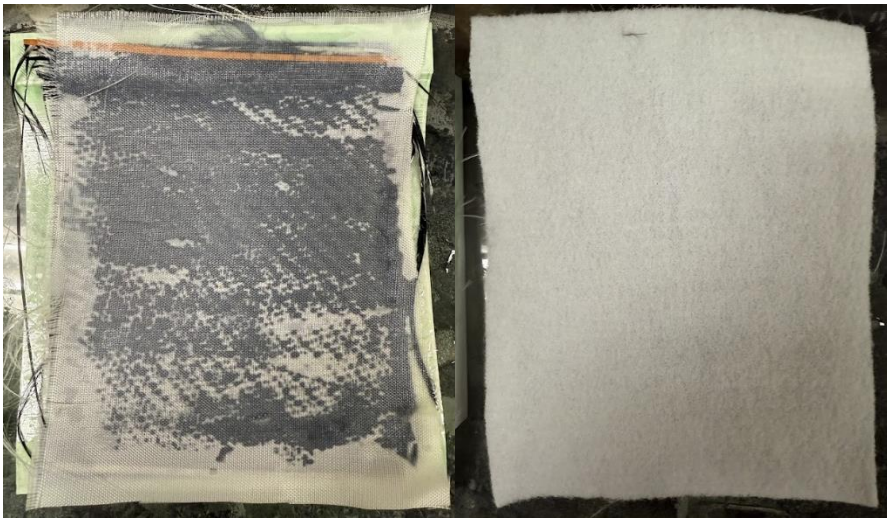


Figure 19: (Left) Peel Ply (Right) Breather Cloth

The thru-bag vacuum connector puck was placed on the breather cloth to serve as the interface for connecting the vacuum pump to the vacuum bag. With this in place, the layup assembly could be placed under vacuum. To form an airtight seal, vacuum seal tape was applied in a continuous loop around the mold on the surrounding surface. The vacuum bag was then positioned over the layup and firmly pressed onto the sealant tape to create a tight seal. Once the vacuum bag was fully secured, a small slit was cut over the vacuum connector puck. This slit allowed the thru-bag vacuum connector to be twisted into place in the puck, allowing for air evacuation from the bag. After assembling the vacuum bag, the vacuum pump was activated. The system was thoroughly checked for leaks and sealed if found. The layup was left under vacuum for 18 hours to ensure complete curing, although the resin hardener has a specified cure time of approximately 12 hours [56]. This extended duration was used as a precautionary measure to ensure a fully cured part. The entire layup and vacuum bag setup are shown in the figure below.

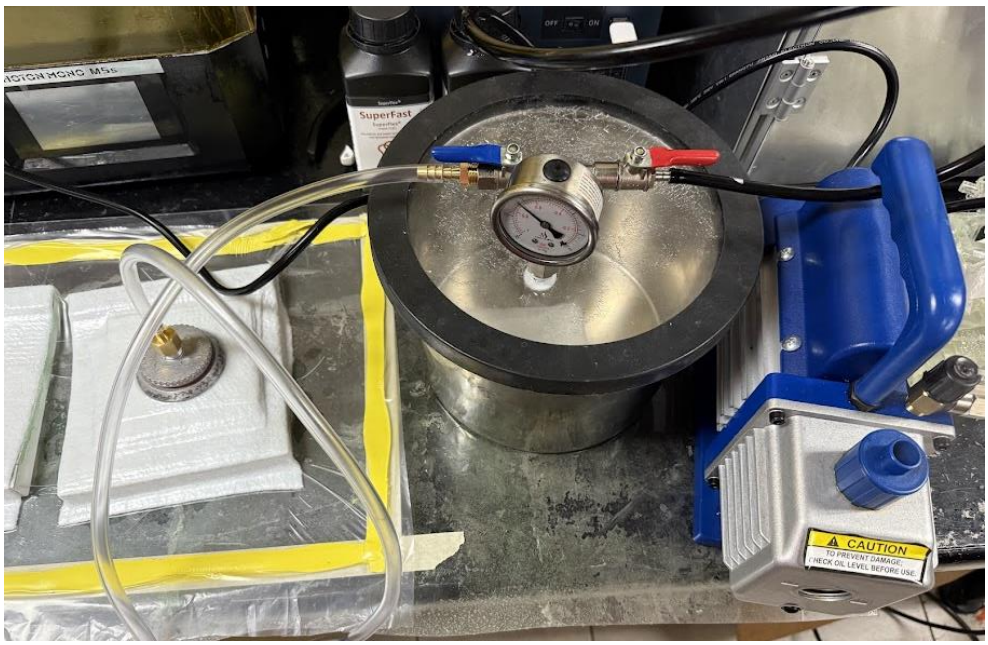
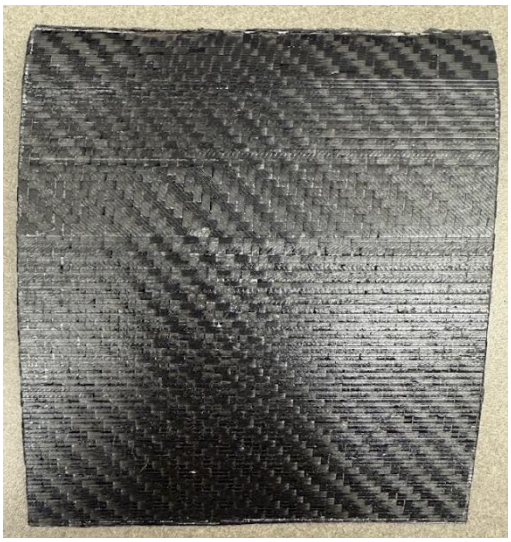
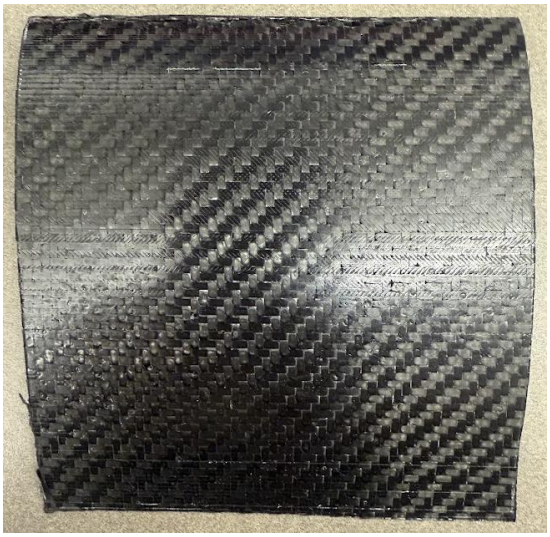


Figure 20: Layup and Vacuum Setup

After 18 hours had passed, the vacuum bag was removed, and the mold was taken out. The carbon fiber part was then separated from the mold. Any residual PVA that remained on the carbon fiber surface was cleaned off using water. Once the part was fully dry, the wing skins were trimmed using a rotary tool to remove any uneven edges and achieve a clean final appearance. The finished wing skins, produced from the three different molds, are shown below.



(a)



(b)



(c)

Figure 21: Wing Skins from (a) Base Mold (b) Sanded Mold (c) Coated Mold

As shown in Figure 21, the difference in surface quality of the carbon is very apparent. The smoother molds produced smoother carbon and in the next section the differences are quantified.

Chapter 3: Surface Roughness Testing

3.1 Surface Roughness Tester



Figure 22: Surface Roughness Tester [58]

The surface roughness measurements were conducted using the surface roughness tester shown in the figure above. This device is a contact-based stylus profilometer with a measurement resolution of 0.001 μm, allowing for highly precise surface texture analysis [58]. The tester operates by moving a stylus across the surface, detecting micro-level deviations in height. These deviations are then used to calculate various roughness parameters to provide a detailed characterization of the surface texture. The relevant roughness parameters are:

Table 4: Surface Roughness Parameters

Parameter	Definition
Arithmetical Mean Roughness (Ra)	Average roughness value calculated as average of absolute deviation from the mean line
Average Maximum Height of Profile (Rz)	The average difference between highest peak and deepest valley across a number of sampling lengths
Mean Width of Profile Elements (RSm)	Average spacing between peaks and valleys

For the CFD simulations, Ra is the most relevant parameter, as it provides an average roughness value that best represents the overall surface texture. Additionally, Rz and RSm will be analyzed to gain a more comprehensive understanding of the surface roughness characteristics, including the peak-to-valley variations and the spacing between surface features.

3.2 Measurement Procedure

The roughness of each mold was measured at every stage of the surface finishing process, including the initial unprocessed surface, after sanding at each grit level, and following the application of the silicone rubber coating with light sanding. Measurements were taken after each step to quantify its effect on surface roughness. To account for potential variations across the mold, roughness was recorded at three distinct locations:

near the leading edge, near the center, and near the trailing edge. The measurements presented are the average of the results from the three locations.

The measurement process for the wing skins followed a similar approach. After the carbon fiber had been trimmed and cleaned, roughness measurements were taken at three distinct locations along the airfoil profile: near the leading edge, the middle, and the trailing edge. This was done again to account for any potential variations in surface roughness across the wing surface.



Figure 23: Wing Skin Roughness Tester Stand

Given the difficulty of using the roughness tester directly on the wing skins, a custom stand was designed and 3D printed to ensure accurate and repeatable measurements. The left side of the stand, as shown in Figure 23, was shaped to match the airfoil profile, providing a stable surface for the wing skin to rest on, with the glossy, smoother side facing upward. The right side of the stand featured three distinct flat sections, each positioned to allow the roughness tester to make measurements at a tangent to the wing skin at the leading edge, middle, and trailing edge locations.

3.3 Roughness Measurements of Molds

To begin, the roughness of the base molds without any surface finishing was measured to assess the surface characteristics resulting from the chosen print parameters.

Table 5: Base Mold Surface Roughness Parameters

Mold	Ra (μm)	Rz (μm)	RSm (mm)
Base	6.145	449.163	0.017
Base (Not Yet Sanded)	6.128	439.023	0.017
Base (Not Yet Coated)	6.018	440.777	0.017

As shown in Table 5, the average Ra, Rz, and RSm values were very similar across all molds, indicating that the mold printing process produces consistent surface quality. The untreated molds exhibited distinct layer lines, resulting in deep ridges and peaks. This is reflected in the high Rz values, which indicate a significant average distance between the highest peaks and deepest valleys. The RSm values represent the average spacing between these peaks and valleys, with a short distance of 0.017 mm suggesting a high frequency of these surface features. Meanwhile, the Ra values describe the overall surface roughness, with a measured roughness of 6 μm, which is relatively high and aligns with the observed mold texture.

The first method explored for reducing mold surface roughness was sanding with a range of grits. After each stage of sanding, the surface roughness was measured, and the results are presented below.

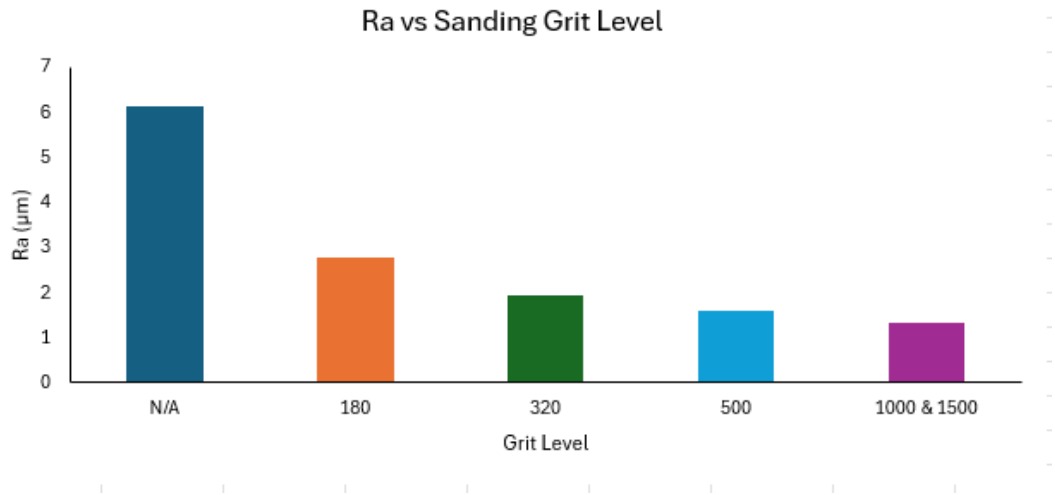


Figure 24: Average Ra of Multiple Sanding Grit Levels

Figure 24 demonstrates that sanding significantly reduces the average roughness of the mold. The "N/A" data point represents the unsanded mold, while the final data point reflects the roughness measurement after sanding with both 1000 and 1500 grit. By the end of the sanding process, the Ra had decreased by 4.807 µm, a reduction of 78.44%. However, the most significant reductions in Ra occurred at coarser grit levels, with diminishing returns as the grit became finer. This suggests that while finer grits help refine the surface, their contribution to further roughness reduction is minimal compared to the initial sanding stages.

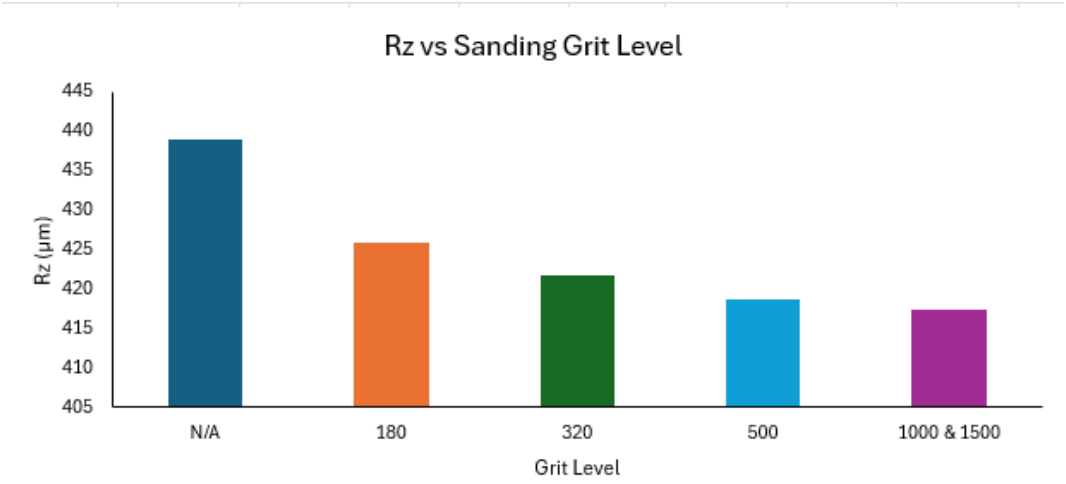


Figure 25: Average Rz at Multiple Sanding Grit Levels

The trend shown in Figure 25 for Rz versus sanding grit level follows a similar pattern to that of Ra. The most significant reductions occurred at coarser grit levels, while the effect diminished as the grit became finer. By the end of the sanding process, the Rz value had decreased by 21.663 µm, representing only a 4.93% reduction. This relatively small change in Rz is due to sanding's inability to completely remove the deep ridges present in the base mold. As observed in Figure 16, these ridges remained visible and could still be felt by touch.

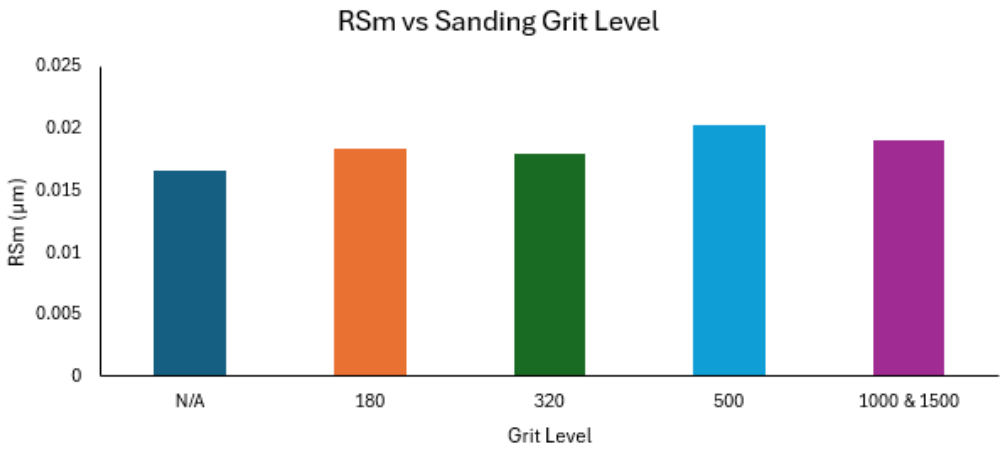


Figure 26: Average RSm at Multiple Sanding Grit Levels

Figure 26 shows that RSm slightly increases as the sanding grit level increases. By the end of the sanding process, RSm had increased by 0.0023 mm, or 14%. This indicates a slight increase in the average spacing between peaks and valleys. This trend is expected, as sanding removes surface irregularities and flattens peaks, leading to a lower frequency and greater distance between these surface features.

The other method of surface treatment of the molds was to apply a silicone rubber coating and lightly sand. The surface roughness of the base mold and the coated mold was measured.

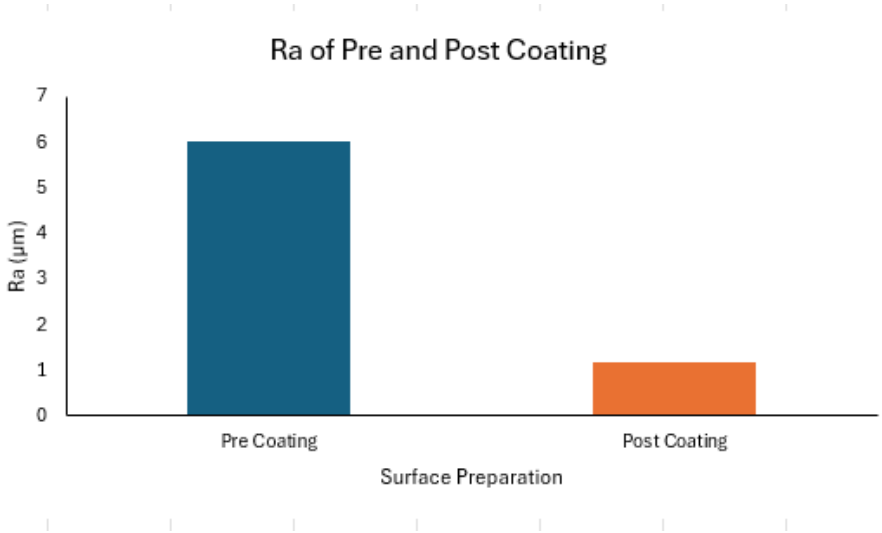


Figure 27: Average Ra of Pre and Post Coating

Figure 27 displays the Ra values before and after the application of the silicone rubber coating. As expected, Ra decreased significantly, dropping by 4.833 µm, which corresponds to an 80.32% reduction. This confirms the effectiveness of the coating in smoothing the mold surface.

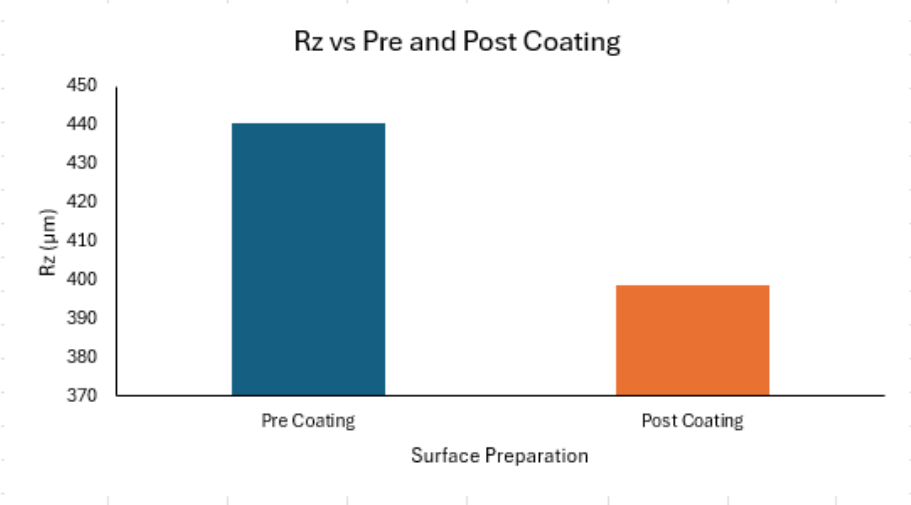


Figure 28: Average Rz of Pre and Post Coating

The coating applied to the mold surface was expected to be more effective at eliminating deep ridges than sanding alone, and the Rz values confirm this. By using a filling material, Rz decreased by 42.17 µm, a reduction of 9.57%. This quantitatively

supports what was observed qualitatively—that the filler material is significantly better at smoothing ridge lines and reducing Rz.

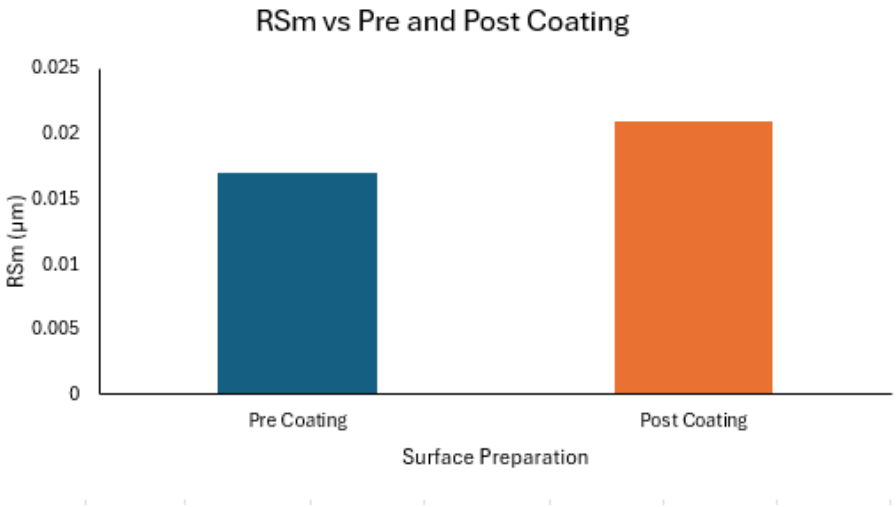


Figure 29: Average RSm of Pre and Post Coating

Coating the mold also effectively reduces the frequency of surface imperfections. This is reflected in the RSm values, which increased by 0.004 mm, or 23.53%, indicating a greater spacing between peaks and valleys as the coating smooths out surface irregularities.

Table 6: Surface Roughness Comparison of Finished Molds

Mold	Ra (µm)	Rz (µm)	RSm (mm)
Base	6.145	449.163	0.017
Sanded	1.321	417.36	.019
Coated	1.184	398.61	.021

Table 6 compares the final surface roughness values of the molds after all surface finishing treatments. Both the sanded and coated molds exhibit significantly lower Ra values than the base mold, with the coated mold achieving a slightly lower Ra than the

sanded mold. Sanding had a moderate effect on reducing Rz; however, due to the persistence of ridge lines, the reduction was not substantial. In contrast, coating the mold had a more pronounced impact on lowering Rz, as the filler material effectively smoothed out these ridge lines. RSm followed a similar trend to Rz, with sanding slightly increasing RSm and coating increasing it further. Based on all three metrics, the coated mold produced the smoothest surface. Both treated molds showed a significant improvement in surface quality compared to the base mold.

3.4 Roughness Measurements of Wing Skins

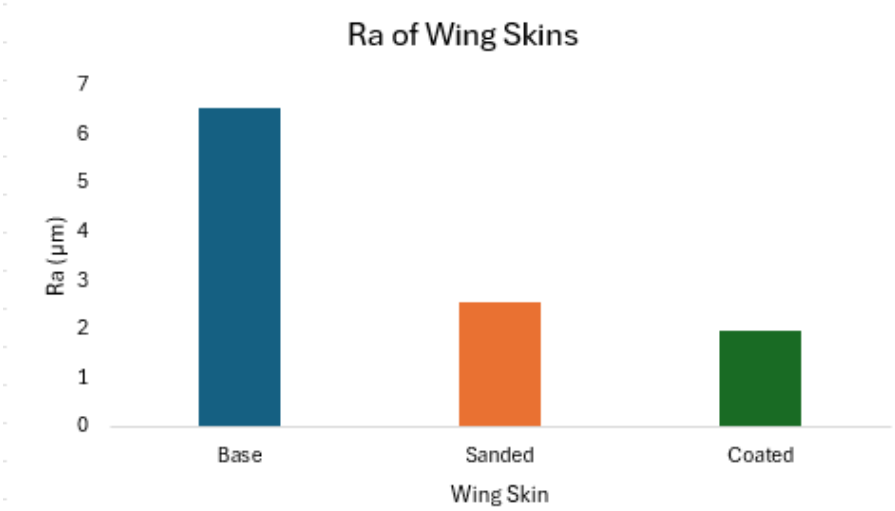


Figure 30: Average Ra of Each Wing Skin

Similar to the relationship observed between Ra and the different mold surface finishes, a similar trend is seen in the surface roughness of the wing skins. The wing skin produced from the base mold exhibited the highest Ra at 6.529 µm, while the wing skins formed using smoothed molds had significantly lower Ra values. Among these, the wing skin from the coated mold had the lowest Ra at 1.951 µm, followed by the wing skin from the sanded mold with an Ra of 2.553 µm.

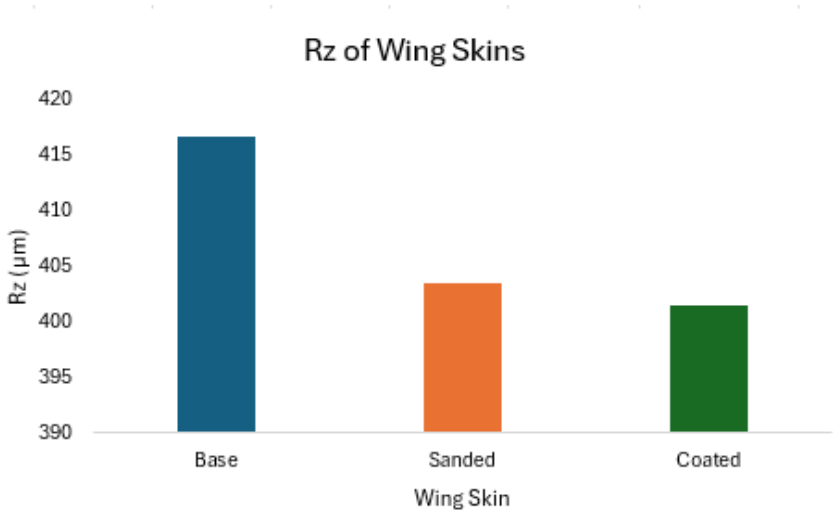


Figure 31: Average Rz of Wing Skins

The Rz of the wing skins shows a small decrease when comparing the base skin to those produced using sanded and coated molds. The base wing skin has an Rz of 416.720 µm, while the skin from the sanded mold has a slightly lower Rz of 403.537 µm, and the skin from the coated mold has an Rz of 401.510 µm. This corresponds to reductions of 13.183 µm and 15.210 µm, respectively, relative to the base skin.

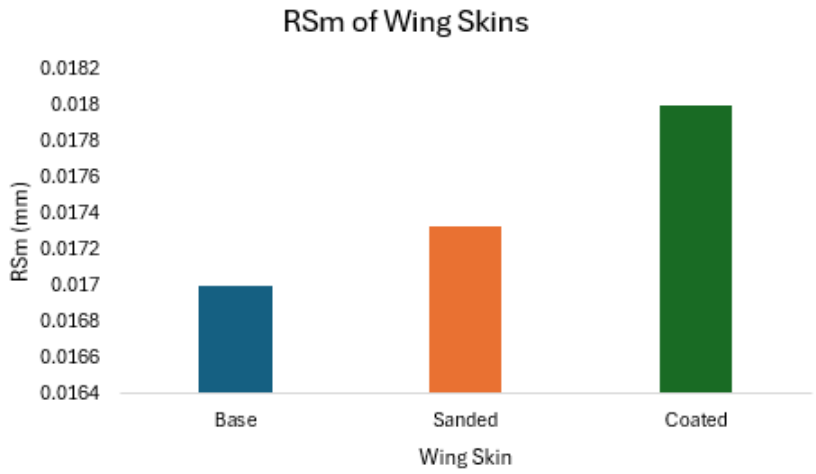


Figure 32: Average RSm of Wing Skins

The frequency of surface imperfections on the wing skins decreases steadily as the molding process progresses from the base to the sanded and then to the coated molds.

This corresponds to an increasing distance between imperfections, indicating an improvement in surface quality. The measured distances between imperfections for the wing skins made from the base, sanded, and coated molds are 0.017 mm, 0.0173 mm, and 0.018 mm, respectively.

Overall, the surface characteristics of the wing skins improve progressively as the mold surface finish is refined from the base to the sanded and finally to the coated mold. The coated mold produces the smoothest wing skin, with the lowest average Ra and Rz values, as well as the largest spacing between surface imperfections, indicating the highest surface quality. While sanding the mold provides noticeable improvements over the base mold, the wing skin was slightly rougher than the one made from the coated mold.

3.5 Mold and Wing Skin Roughness Comparison

Since the surface quality of the mold directly affects the surface finish of the carbon wing skins, the roughness values of both were compared to identify potential relationships. Analyzing the correlation between mold roughness and the resulting wing skins helps assess the impact of mold sanding and coating, quantifying how these treatments improve surface quality of the final product.

Table 7: Mold and Wing Skin Surface Roughness Parameters

	Base		Sanded		Coated	
Roughness Parameter	Mold	Wing Skin	Mold	Wing Skin	Mold	Wing Skin
Ra (μm)	6.145	6.529	1.321	2.553	1.184	1.951
Rz (μm)	449.163	416.72	417.36	403.537	398.607	401.51
RSm (μm)	0.0173	.017	0.019	.0173	0.021	.018

Comparing the surface roughness results across the base, sanded, and coated molds and their corresponding wing skins reveals a clear trend in surface quality improvement. The most significant decrease in roughness occurs when comparing the sanded mold to the base mold, while the additional reduction from sanding to coating is smaller but still notable. Across all cases, the molds are smoother than the wing skins produced from them, as seen in the Ra values, where each wing skin has a higher Ra than its corresponding mold. The Rz values, however, are lower for the wing skins than the molds, except in the coated set, where the wing skin exhibits a slightly higher Ra. Additionally, the RSm values indicate that the spacing between surface imperfections is greater on the molds than on the wing skins.

These results suggest that imperfections on the mold surface are transferred and, in some cases, amplified onto the wing skin during the layup process. This effect may be inherent to hand layups, where inconsistencies and minor errors arise due to the manual application of materials. Although the final wing skin surface does not perfectly replicate the mold's roughness, the overall trend remains consistent. Coating the mold results in the smoothest mold and wing skin, followed by sanding, with the base mold producing the roughest surfaces.

Chapter 4: CFD Simulations

4.1 Simulation Setup

This section details the setup of the CFD simulations used to analyze the aerodynamic effects of surface roughness on carbon fiber wing skins fabricated from 3D-printed molds. Using the measured Ra values from the different wing skins, the simulations evaluate how the Ra values influence key aerodynamic performance metrics, including C_L and C_D. By incorporating real roughness data, the simulations provide an accurate representation of how manufacturing-induced surface imperfections impact aerodynamic performance. Ansys Fluent was used to conduct the simulations of a wing with varying surface roughness.

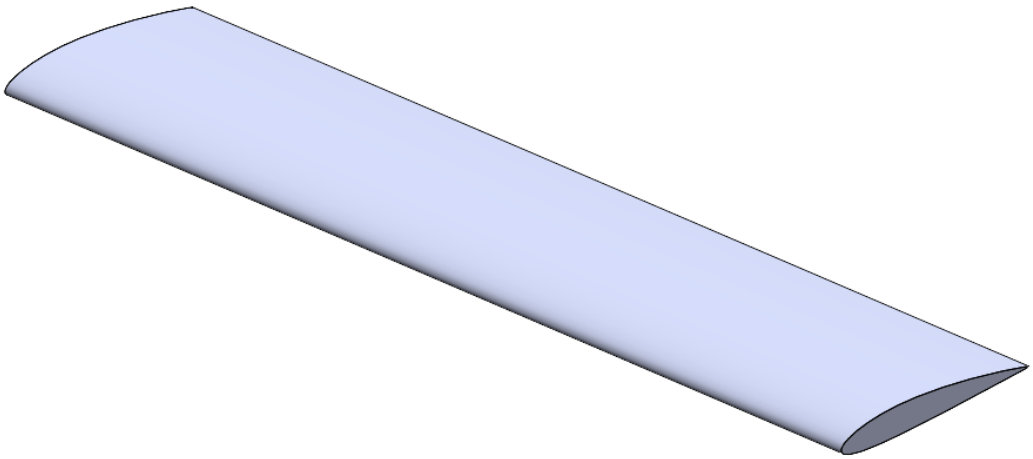


Figure 33: CAD Model of Wing for CFD

The wing model used for the CFD simulations is a rectangular wing featuring a NACA 2412 airfoil, designed with dimensions that maintain an aspect ratio of 7.5, similar to aircraft that utilize this airfoil [48-49]. The span is 1.5 meters, and the chord length is 0.2 meters, making it a scaled-down version rather than the same size of an existing wing. These reduced dimensions were intentionally chosen to minimize computational

demands while still preserving the aspect ratio. By maintaining the same aspect ratio, the aerodynamic performance remains representative of a full-scale wing, ensuring that any changes in lift, and drag are not due to aspect ratio differences.

To further reduce computational demands, only half of the wing will be simulated using symmetry boundary conditions to replicate the behavior of a full-span simulation. This approach reduces computational time and resource usage while ensuring that the simulated aerodynamic performance accurately reflects that of the complete wing. Since C_L and C_D are normalized by wing area, the recorded values will remain consistent regardless of whether the entire wing or only a symmetrical half is simulated.

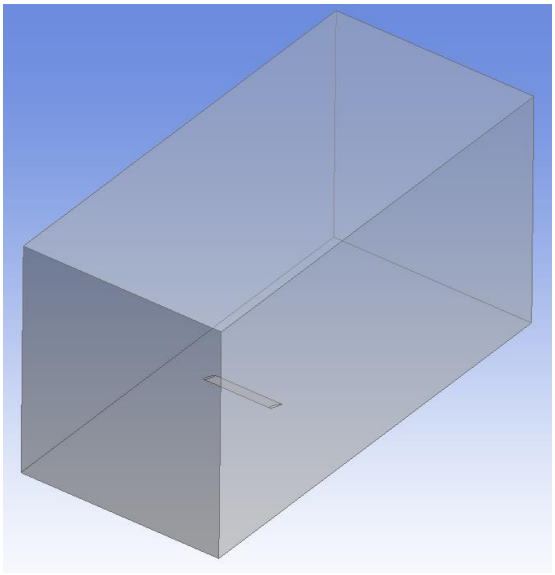


Figure 34: CFD Fluid Volume

The first step in the CFD simulation is to define the fluid volume, which represents the region where airflow enters, interacts with the wing, and exits. This domain is modeled as a rectangular prism, with each face assigned specific boundary conditions to ensure an accurate representation of real-world aerodynamic behavior.

Table 8: Boundary Conditions of Fluid Volume

Surface	Boundary Condition	Purpose
Front Face	Velocity Inlet	Defines incoming airflow velocity and direction
Back Face	Pressure Outlet	Allows air to exit while maintaining atmospheric pressure
Symmetry Face	Symmetry	Reduces computation time by assuming symmetric flow behavior
Top, Bottom, and Outer Face	Far-Field	Simulates undisturbed airflow at a distance from the wing
Wing Surface	Wall	Represents the solid, no-slip boundary where airflow interacts with the wing

The fluid volume was sized to ensure accurate simulations while minimizing computational time and resource usage. Its dimensions were determined using multiples of the wing's chord length. The front, top, and bottom faces were positioned at 10 times the chord length, providing sufficient space for airflow to develop. The outer face was set at 2 times the wingspan from the wingtip to allow for lateral flow expansion. The back face was placed 20 times the chord length downstream to ensure proper wake development and prevent artificial pressure gradients [59-60]. Finally, a symmetry boundary was applied along the wing's centerline, enabling symmetric flow behavior.

After defining the fluid volume, the next step was to generate the computational mesh. The edge and face sizing for the wing and surrounding fluid domain were determined based on recommended percentages of the wing's chord length [60], ensuring

appropriate resolution in critical regions. The overall element size for the fluid volume was carefully chosen to balance accuracy and computational efficiency, keeping it fine enough to capture aerodynamic effects while avoiding excessive simulation time.

The boundary layer meshing was the most complex of the process, as it ensures the accurate resolution of near-wall flow behavior. Proper boundary layer meshing is essential for correctly capturing boundary layer development, transition, and separation. It enables precise modeling of how Reynolds number (Re) variations, changes in angle of attack, and surface roughness influence flow characteristics.

To initiate the boundary layer meshing process, the Re for the simulation must first be determined. To ensure a comprehensive analysis, the wing will be simulated under three distinct Re: 300,000, 3,100,000, and 5,400,000. The lower Re of 300,000 represents the operating conditions of small-scale aerodynamic applications such as RC aircraft and FSAE race cars, where low-speed aerodynamics play a significant role. The higher Re of 3,100,000 and 5,400,000 were chosen because these values correspond to the operating regimes of small general aviation aircraft and certain UAVs. They are also Re that airfoil data is commonly reported at [61]. With the Re selected, the succeeding calculations can be completed.

$$Re = \frac{\rho v c}{\mu}$$

$$C_f = \frac{0.026}{Re^{\frac{1}{7}}}$$

$$\tau_w = \frac{C_f \rho U_\infty^2}{2}$$

Using the selected Re and standard sea-level conditions, the flow velocity can be determined. From this, the skin friction coefficient is calculated as a function of Re, allowing for the computation of wall shear stress. With the wall shear stress known, the appropriate y^+ value must be selected to determine the placement of the first grid point in the prism layer.

y^+ is a dimensionless wall distance used in CFD to assess whether the near-wall mesh resolution is sufficient to capture boundary layer effects accurately. Since the primary objective of these simulations is to properly model the viscous sublayer, a y+ of 1 is ideal. Additionally, a y^+ of 1 aligns with the turbulence models used in these simulations, ensuring accurate near-wall flow predictions [60]. With this, the first cell height Δs can be calculated.

$$\Delta s = \frac{y^+ \mu}{\frac{\sqrt{\tau_w}}{\rho}\rho}$$

$$\delta_{99} = \frac{0.37c}{Re^{0.2}}$$

With the calculated Δs and an approximated total boundary layer thickness (δ_{99}), the growth rate (G) of the prism layers (N) can be calculated. The growth rate of 30 prism layers was used as that has been shown to be sufficient [60].

$$\delta_{99} = \frac{1 - G^N}{1 - G}$$

Completing these calculations results in the following parameters used for the CFD simulations for each RE.

Table 9: Boundary Layer Meshing Parameters

Re	Δs (m)	δ_{99} (m)	G
300,000	1.44E-05	0.005940288	1.147374
3,100,000	1.65E-06	0.003723569	1.2322972
5,400,000	9.35E-07	0.003296528	1.2544265

Using the prism layer meshing parameters at a Re of 300,000 the mesh around the wing can be shown in Figure 35.

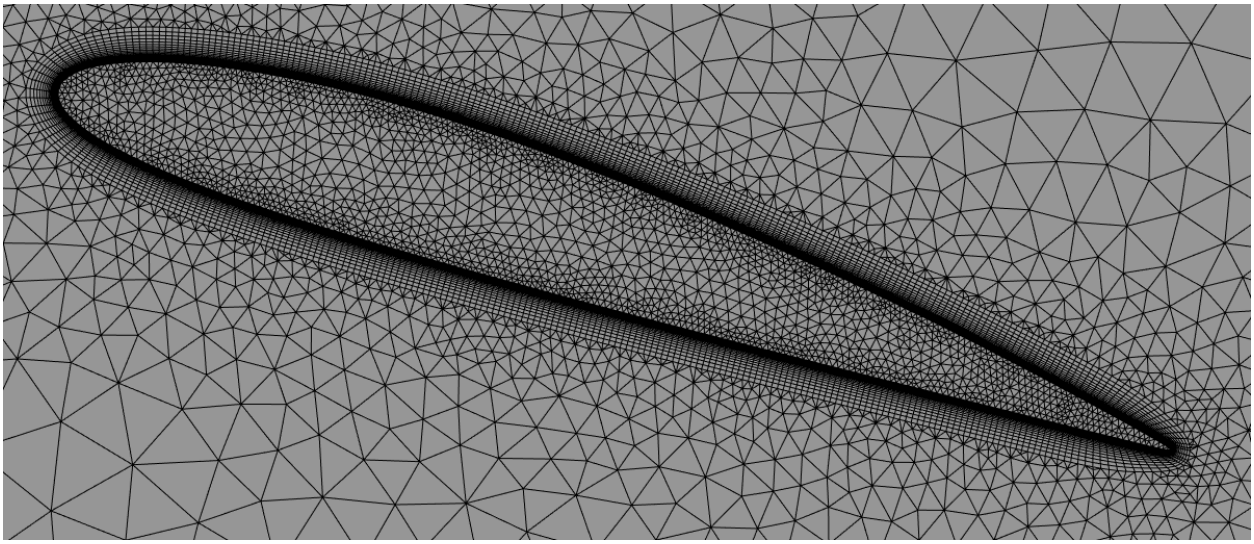


Figure 35: CFD Mesh

The prism layer mesh around the airfoil consists of layers of rectangular cells that increase in thickness to accurately capture the boundary layer. Surrounding these, triangular cells grow in size further from the wing to reduce computational cost while maintaining solution accuracy. This mesh contains 946,458 nodes and 2,489,951 elements.

With the meshing complete, the last thing to do was to apply the values required for each boundary condition. For the velocity inlet, to specify the velocity of the air entering the fluid domain, the velocity calculated from the Re was used. To apply a surface roughness to the wing wall boundary condition, a sand-grain roughness (k_s) was needed. Since the surface roughness tester does not measure that, a method to convert Ra to k_s was used. Based on experimental results Ra was correlated to k_s with the following conversion factor [62].

$$k_s = 5.863 * Ra$$

Table 10: Converted Ra to Sand Grain Roughness

Wing Skin	Ra (μm)	k_S (μm)
Base	6.529	38.279
Sanded	2.553	14.970
Coated	1.951	11.438

With these values, the simulation setup is complete and the CFD simulations for every roughness can be run at each Re and angle of attack (AOA).

4.2 CFD Results: Coefficient of Lift and Drag

For each simulation, the C_L and C_D of the wing were recorded and plotted as functions of the AOA, categorized by surface finish.

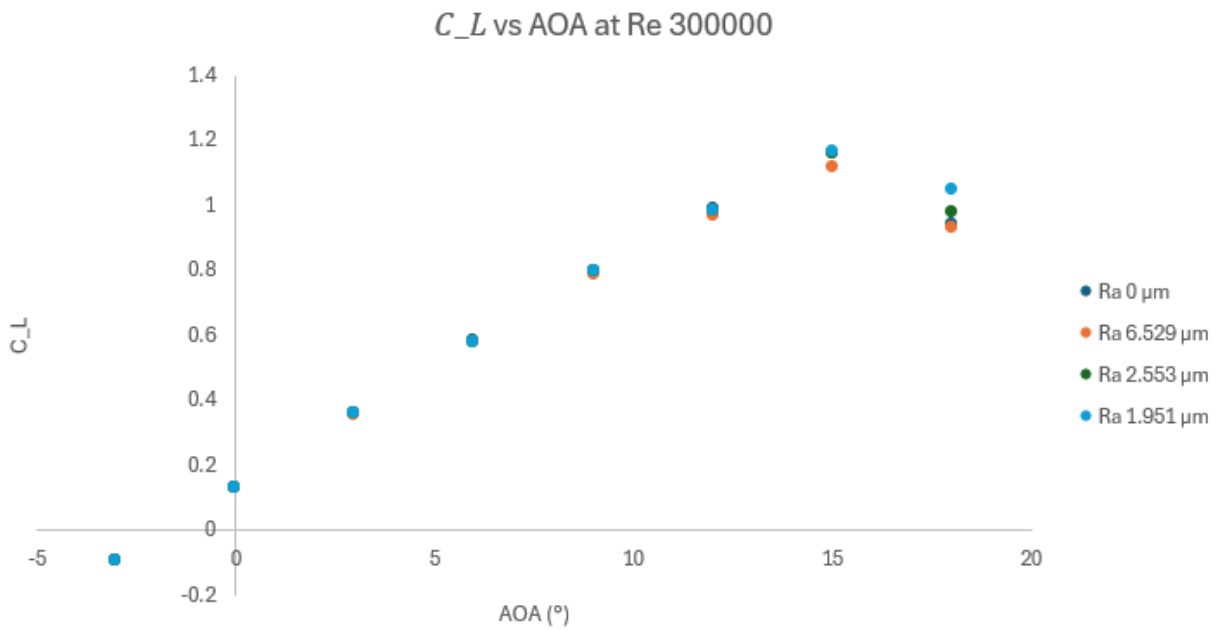


Figure 36: C_L vs AOA at Re 300,000

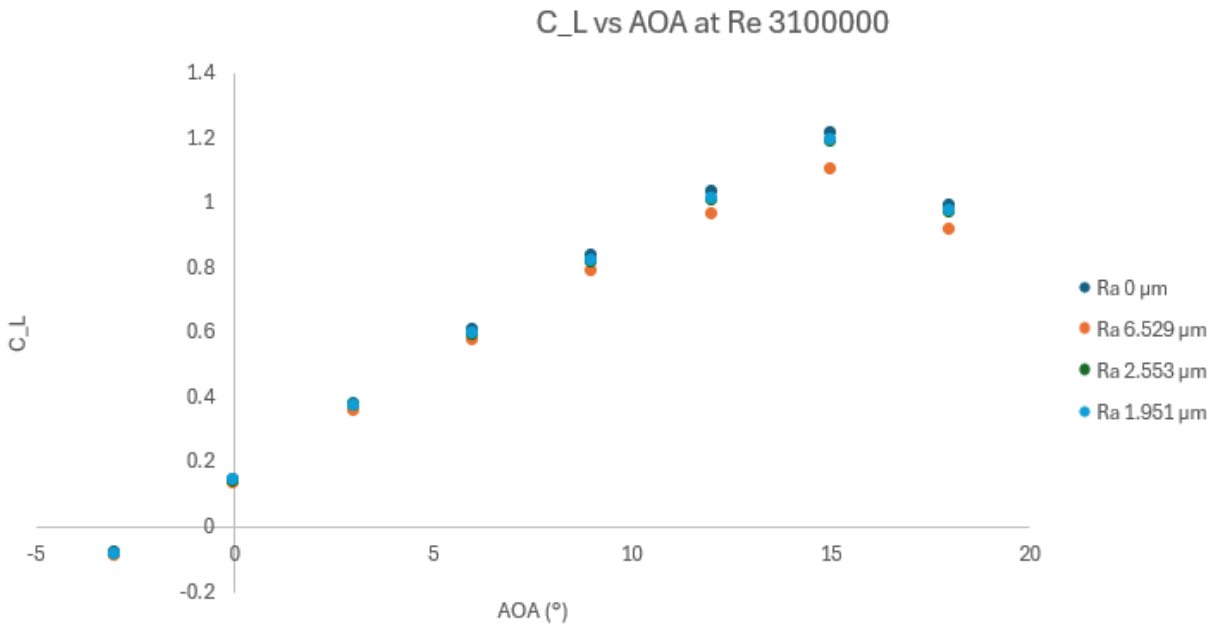


Figure 37: C_L vs AOA at Re 3,100,000

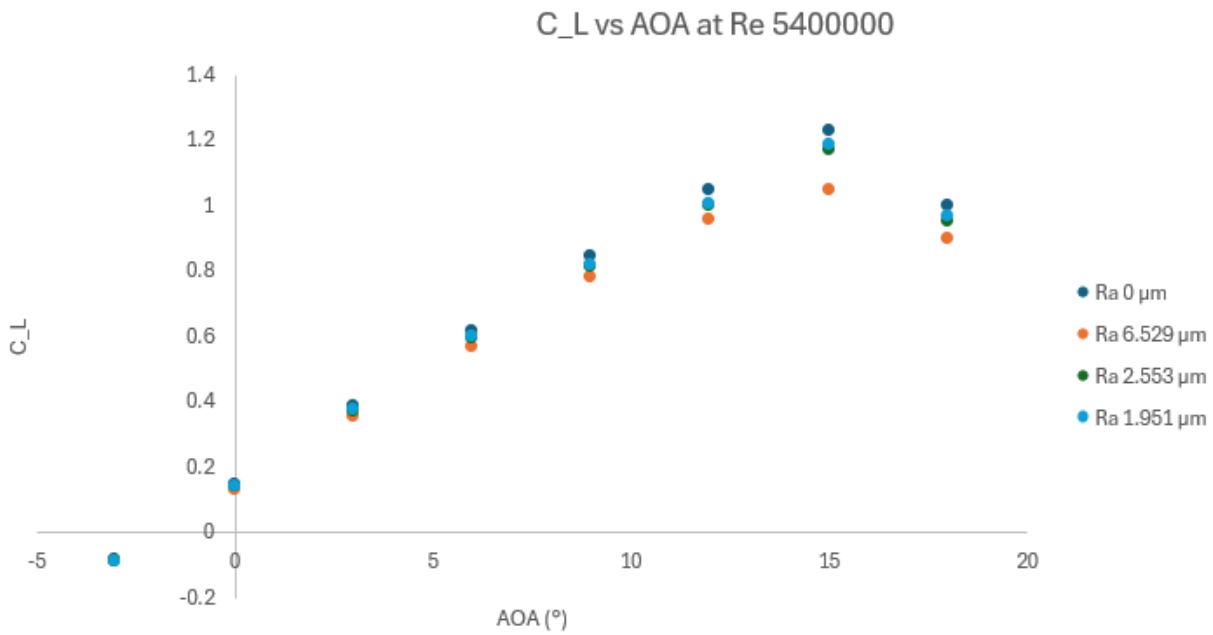


Figure 38: C_L vs AOA at Re 5,400,000

The values for an Ra of 0 µm correspond to the perfectly smooth surface of the imported CAD model, serving as a baseline for comparison against the roughness of the fabricated wing skins. It has the highest C_L across all AOA at Re of 3,100,000 and 5,400,000. At the lowest Re of 300,000, the Ra 0 µm wing maintains the highest C_L up to 15°, but at this AOA, the Ra 1.951 µm wing slightly surpasses it, achieving a C_L that is 0.3% higher. At 18°, where airflow over the upper surface of the wing separates, the Ra 2.553 µm and Ra 1.951 µm wings achieve higher C_L values by 3.89% and 11.03%, respectively, compared to the smooth surface. For all other combinations of Re and AOA, the Ra 1.951 µm wing consistently has the second highest C_L, followed by the Ra 2.553 µm wing in third. Across all Re and AOA conditions, the Ra 6.529 µm wing has the lowest C_L.

The change in C_L at pre stall conditions is also correlated with Re. As the Re increases the reduction in C_L increases as well. At Re 300,000 the average decrease in C_L

is 0.845 % while at Re 5,400,000 the average decrease is 5.853 %. As AOA increases the reduction in C_L also increases.

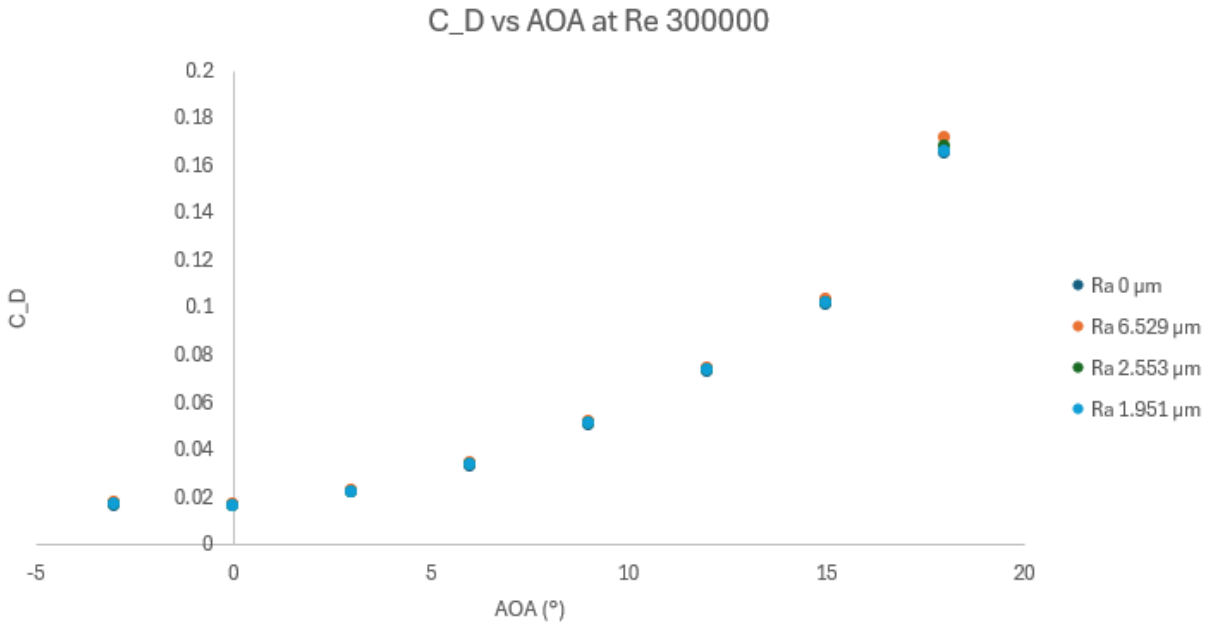


Figure 39: C_D vs AOA at Re 300,000

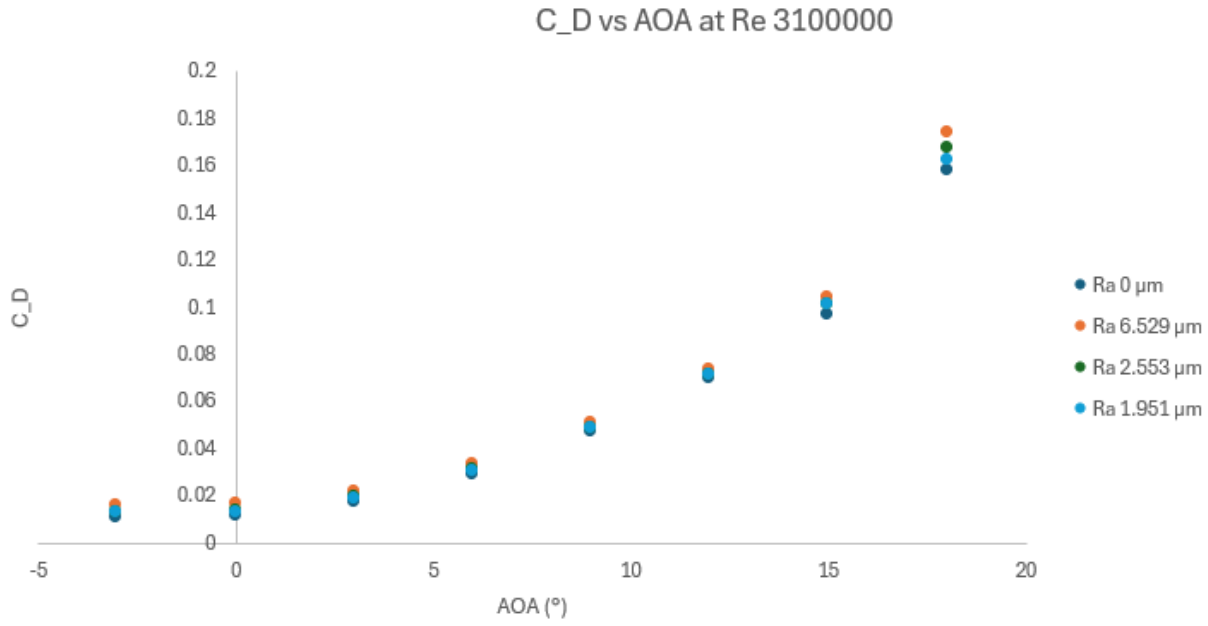


Figure 40: C_D vs AOA at Re 3,100,000

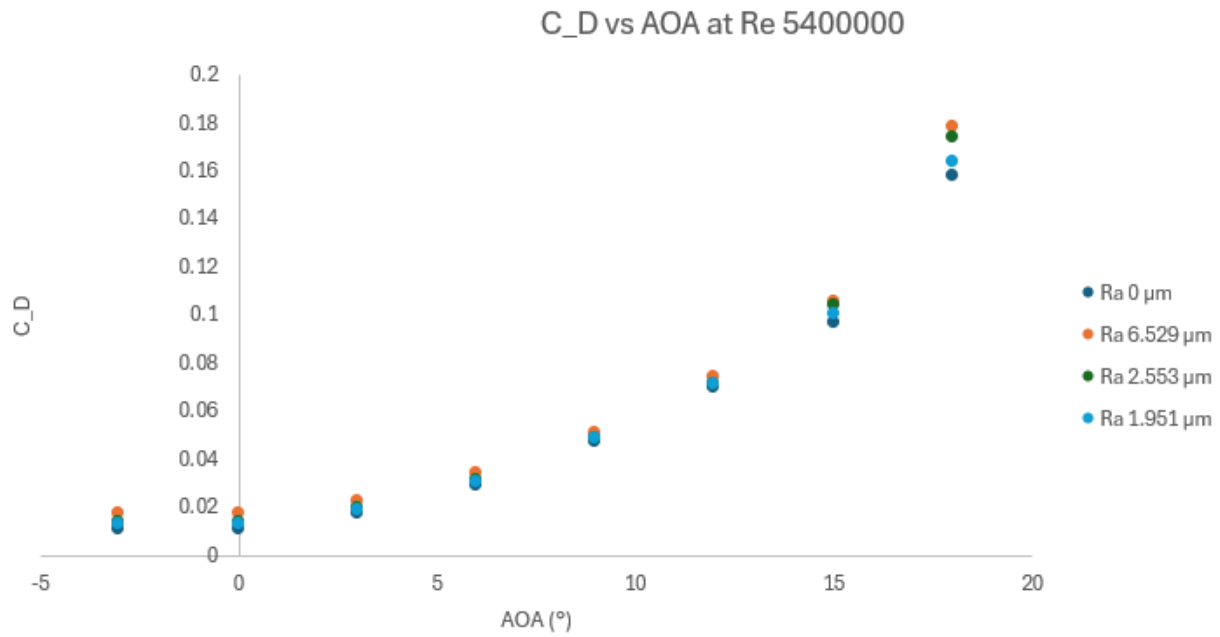


Figure 41: C_D vs AOA at Re 5,400,000

The results for C_D show similar trends to those seen in the C_L results. The wings with the lowest C_D to the highest are Ra 0 μm, Ra 1.961 μm, Ra 2.553 μm, and Ra 6.529 μm. At no point is there a combination of AOA and Re where there is a C_D lower than the corresponding value for the Ra 0 μm baseline.

As the Re increases from 300,000 to 5,400,000 the increase in C_D increases as well. At the lowest simulated Re the average pre stall C_D increase is 1.85% while at the highest Re it is 13%. As the AOA increases the increase in C_D decreases until stall. However, after stall the C_D increase reaches a maximum.

4.3 CFD Results: Boundary Layer Analysis

The effect of surface roughness on C_L and C_D stems from its impact on the boundary layer. Variations in surface height disturb the airflow over the wing, potentially inducing an earlier transition from laminar to turbulent flow or even causing flow separation,

which can reduce lift and increase drag. To better visualize these effects, boundary layer images were generated for analysis.

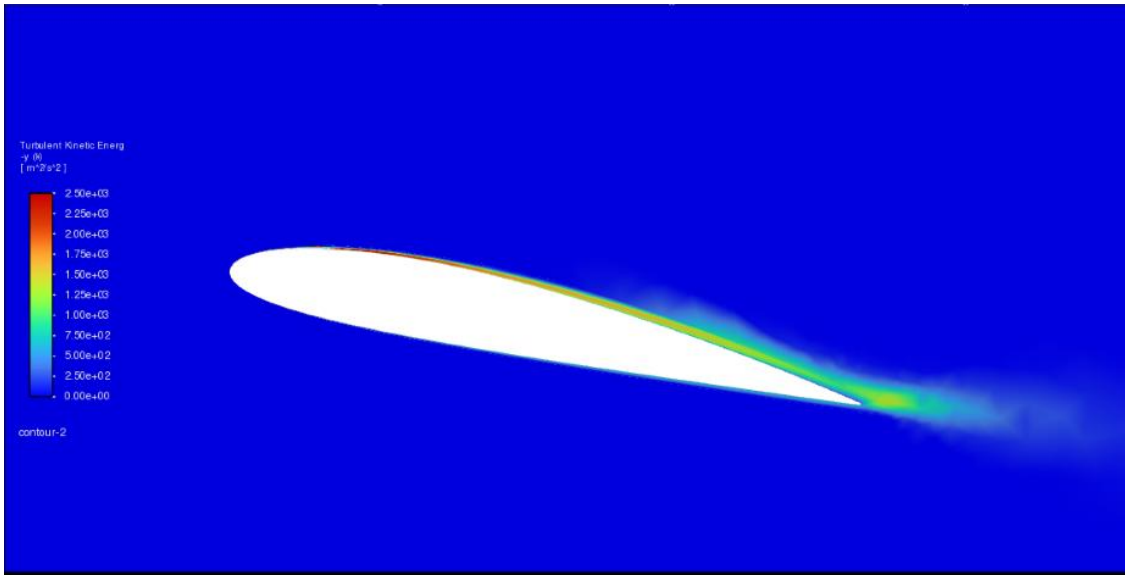


Figure 42: Turbulent Kinetic Energy Contour of Ra 0 μm Wing

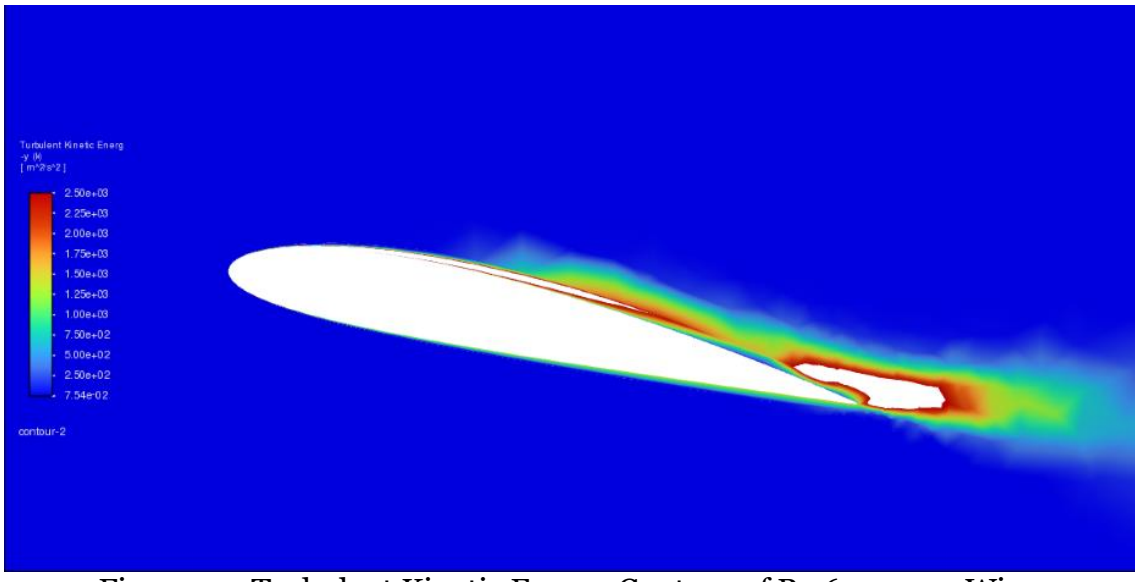


Figure 43: Turbulent Kinetic Energy Contour of Ra 6.529 μm Wing

The images above display Turbulent Kinetic Energy (TKE) contours around the wing at the same AOA of 12° and Re 5,400,000 but with different surface roughness levels. Figure 42 represents a perfectly smooth wing, while Figure 43 depicts the roughest

wing simulated. A comparison of the two reveals a clear difference in TKE distribution along the wing surface.

In Figure 42, TKE gradually increases along the wing as the boundary layer naturally transitions from laminar to turbulent. In contrast, Figure 43 shows a much more rapid increase in TKE, with turbulence developing earlier and spreading more extensively. This indicates an accelerated transition to a turbulent boundary layer, which ultimately leads to flow separation near the trailing edge. This change in boundary layer behavior explains why increased surface roughness reduces lift, and increases drag. These images also demonstrate why surface roughness has a larger impact on aerodynamic performance at higher Re.

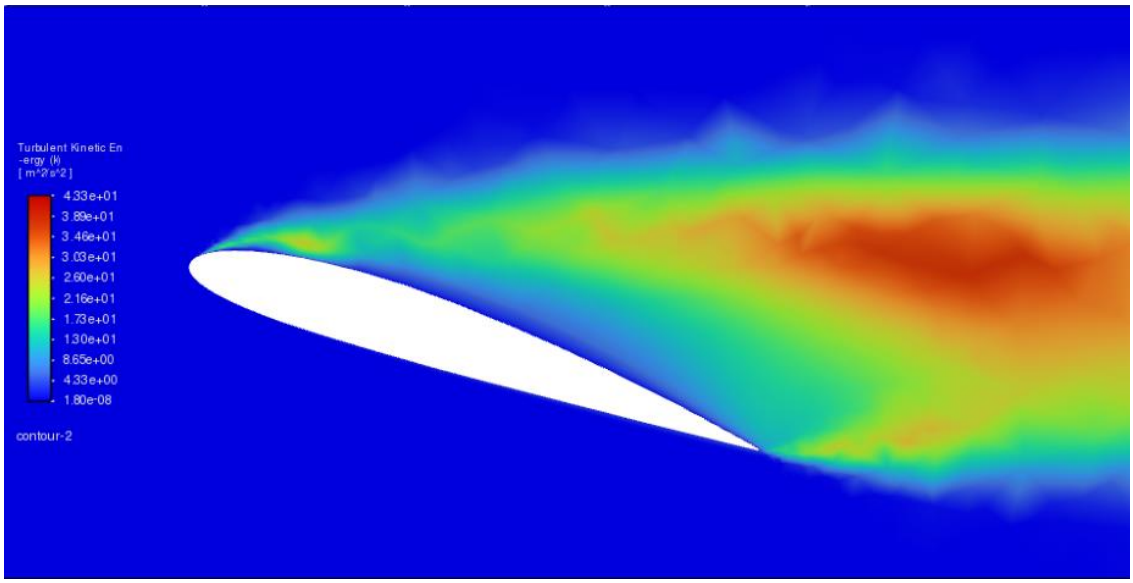


Figure 44: TKE Contour of Ra 0 µm Wing at Re 300,000 and AOA 18°

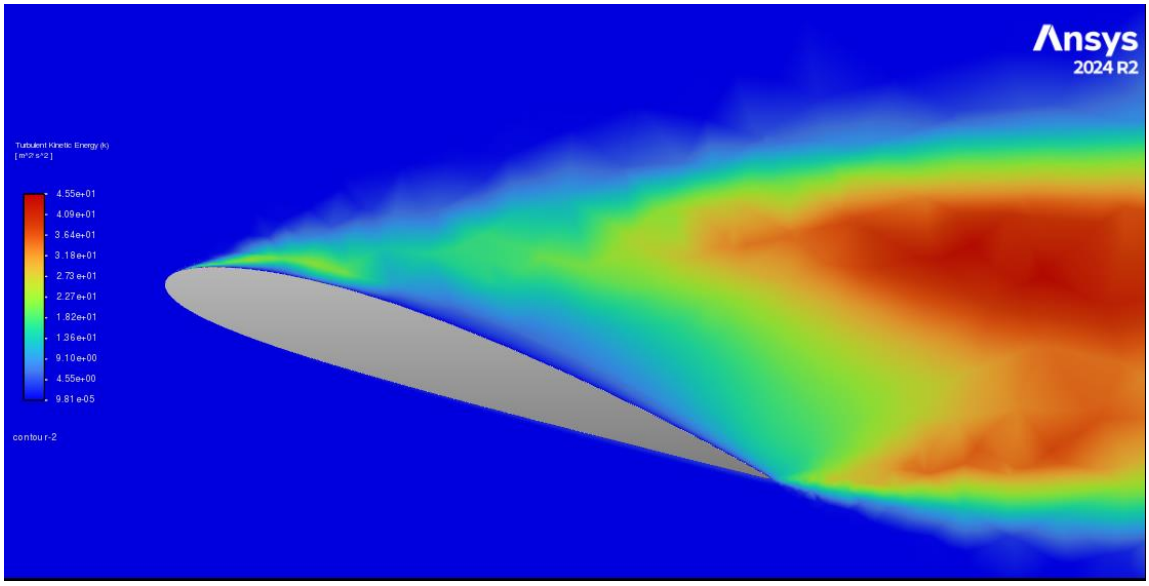


Figure 45: TKE Contour of Ra 1.951 µm Wing at Re 300,000 and AOA 18°

Figures 44 and 45 both depict wings at a stalled AOA, but the wing with an Ra of 1.951 µm achieves a higher C_L than the wing with an Ra of 0 µm. While surface roughness can disrupt airflow and introduce turbulence, this is not always detrimental. In cases where the boundary layer has already separated, a small amount of surface roughness can help re-energize it, delaying flow separation and allowing it to remain attached longer. This effect can enhance lift but also leads to increased drag. Comparing the two images, the boundary layer remains attached for a longer distance near the leading edge in Figure 45 than in Figure 44, illustrating the role of surface roughness in modifying boundary layer behavior.

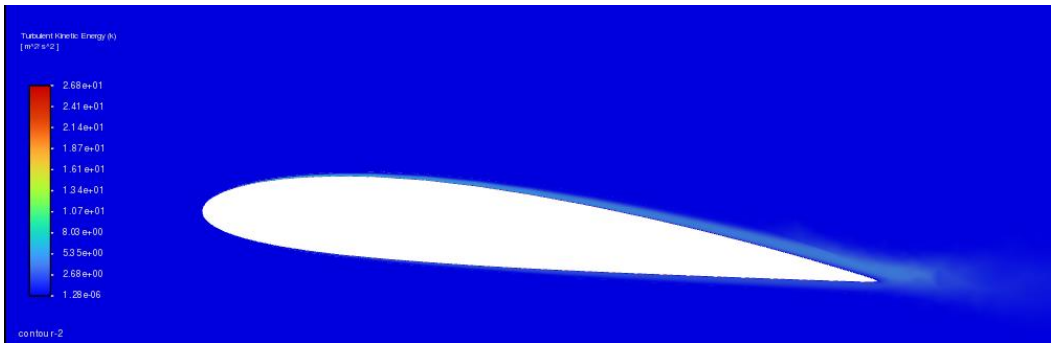


Figure 46: TKE Contour of Ra 0 μm wing at Re 300,000 and 6° AOA

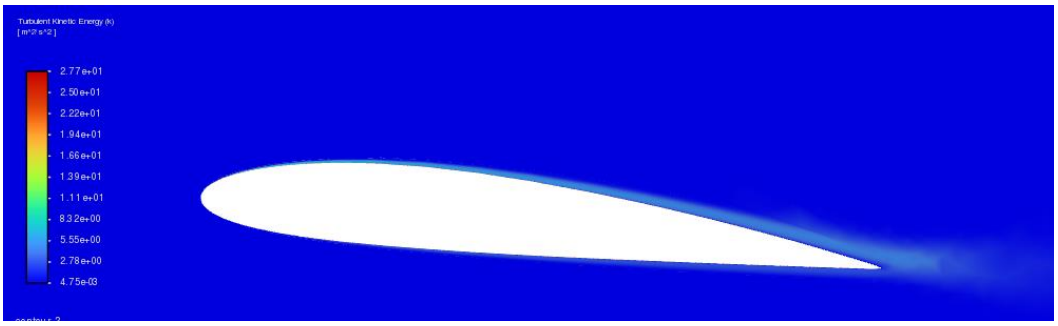


Figure 47: TKE Contour of Ra 6.529 μm wing at Re 300,000 and 6° AOA

Surface roughness was also found to have little effect at the lowest Re of 300,000. This can be understood by analyzing Figures 46 and 47. Despite the significant difference in surface roughness between the two wings, the boundary layer shows no noticeable changes in TKE. This suggests that at this Re, the influence of surface roughness on turbulence generation is minimal, explaining the small difference in aerodynamic performance between the two cases.

The effect of surface roughness is Re-dependent due to changes in boundary layer thickness. As shown in Table 9, the maximum boundary layer thickness at each Re decreases as Re increases. When the boundary layer becomes thinner, the relative height difference between the boundary layer and surface roughness decreases, making the roughness more effective at disrupting the flow and increasing its influence on aerodynamic performance.

Chapter 5: Conclusions and Future Work

5.1 Summary of Findings

The objective of this study was to evaluate the impact of surface roughness—introduced through varied 3D-printed mold finishes—on the aerodynamic performance of CFRP wing skins. By integrating practical manufacturing methods with aerodynamic analysis, this work aims to define viable surface finish tolerances that balance performance with fabrication time and effort.

Multiple molds were printed using PETG, each subjected to different post-processing treatments to produce a range of surface finishes. These molds were then used in wet layup fabrication to create CFRP wing skins, which were measured for surface roughness. The resulting roughness values were incorporated into CFD simulations to evaluate aerodynamic performance across different Re and AOA.

The study examined the effectiveness of mold surface finishing techniques in reducing roughness and how those reductions translated to the resulting CFRP surfaces. Results confirmed a similar transfer of mold roughness to the CFRP wing skins and showed that surface roughness had a measurable impact on both lift and drag. The sensitivity of aerodynamic performance to roughness was also found to vary with Reynolds number and AOA.

With these findings, the 3D printing process parameters can now be revisited to identify optimal mold surface roughness targets. This enables more deliberate mold production strategies that minimize aerodynamic penalties while streamlining the manufacturing process based on the performance requirements of specific applications.

5.2 Mold Surface Roughness Targets

The CFD simulations conducted at a Re number of 300,000 showed that prior to stall, the differences in lift reduction and drag increase between wing surfaces with roughness values of Ra 1.951 μm, 2.553 μm, and 6.529 μm were minimal. Across this pre-stall regime, all three wings performed similarly, indicating that moderate surface roughness does not significantly affect aerodynamic efficiency under attached flow conditions. However, in post-stall conditions, surface roughness had a more noticeable effect. The two smoother wing surfaces exhibited significantly better lift recovery compared to the roughest surface, which failed to regain as much lift after flow separation.

Therefore, at a Re of 300,000, surface roughness has a negligible impact on aerodynamic performance in the pre-stall regime but becomes more influential post-stall. This suggests that for low Reynolds number applications operating below stall—such as RC aircraft, FSAE competition cars, or other small, slow-flying platforms, surface smoothness requirements can be relaxed to prioritize faster or more efficient mold production. Conversely, in cases where post-stall behavior is critical, smoother mold surfaces may be necessary to maintain aerodynamic performance.

The CFD simulations conducted at higher Re of 3,100,000 and 5,400,000 produced more definitive results compared to the lower Re case. Across all angles of attack, the smoother wing surfaces consistently outperformed the rougher ones, exhibiting significantly smaller reductions in lift and increases in drag.

These findings indicate that in high-Re applications—such as larger aircraft or faster, larger drones, the surface quality of aerodynamic components cannot be compromised. Print parameters and post-processing techniques, including layer height

and finishing treatments, must be optimized to minimize surface roughness. The aerodynamic penalties associated with rough surfaces at these conditions are too severe to justify manufacturing shortcuts.

5.3 Mold Print Parameters and Surface Finishing

Given that the wing skin produced from the base mold performed similarly to the one made from the coated mold at a Reynolds number of 300,000, a mold with a surface roughness near the base mold's Ra of 6.145 μm is sufficient for low-Re applications. The base mold was printed using standard FDM settings, with certain parameters modified to improve mechanical strength without significantly impacting surface quality. Among the remaining settings, layer height is the most influential on surface roughness; reducing it could yield a smoother surface but at the expense of increased print time.

Since the base mold already demonstrated acceptable aerodynamic performance, further post-processing—such as sanding or epoxy coating—is unnecessary for applications operating in this Reynolds number range. These finishing steps add considerable manufacturing time without delivering proportional aerodynamic benefits. Therefore, for low-speed, cost-sensitive use cases, the print settings used in this study offer an effective compromise between performance and efficiency. If improved surface quality is needed, lowering the layer height remains a straightforward solution.

For aerodynamic surfaces operating at higher Reynolds numbers of 3,100,000 and 5,400,000, achieving the smoothest possible mold surface is critical for maximizing aerodynamic performance. In this study, the smoothest mold was created by applying a silicone rubber coating and sanding up to 1500 grit, resulting in a surface roughness of

Ra 1.184 μm. Even with this level of effort, CFD results suggest that aerodynamic surfaces would continue to benefit from an even smoother finish.

While coatings and sanding can significantly reduce surface roughness, they may not fully eliminate the influence of the underlying printed texture. Reducing the layer height during printing produces a smoother base surface, which reduces the burden on post-processing to correct surface imperfections. This, in turn, enhances the effectiveness of surface finishing techniques—such as coatings and sanding—resulting in a lower final surface roughness and improved aerodynamic performance. Additionally, the use of a higher-resolution 3D printer may further improve the baseline surface quality of the mold. Incorporating powered sanding tools could also make the surface finishing process more efficient and consistent

5.4 Future Work

To continue the work of this thesis, there are multiple directions for expanding upon the findings and further verifying the conclusions.

The CFD simulations in this study were limited to a finite wing without any attached body or external flow influences. Future simulations could explore how surface roughness affects other aerodynamic geometries and use cases. Applying measured roughness values to models of full aircraft models, wind turbine blades, or propeller geometries could offer additional insight into how surface finish influences performance in different flow regimes. These cases may reveal different sensitivities to roughness based on geometry, flow attachment, and operating conditions. Additionally, future studies could evaluate more performance parameters beyond just lift and drag, such as pressure distribution, flow separation location, or moment coefficients.

This study also evaluated only three levels of mold surface finish, which represents a small subset of the possible finishes achievable with various manufacturing techniques. Future work could explore a broader range of post-processing methods—including chemical smoothing and other coatings—to assess their effectiveness in reducing mold surface roughness. Using higher-quality, industrial-grade 3D printers could be more realistic and help establish the limits of surface finish quality achievable through printing alone, potentially reducing the need for extensive post-processing.

Finally, experimental validation through wind tunnel testing or other physical experiments could provide real-world aerodynamic data to compare with CFD predictions. In parallel, developing more automated or scalable surface finishing processes—such as powered sanding tools, robotic finishing, or spray-based smoothing methods—could improve manufacturing efficiency and consistency.

References

[1] Dipen Kumar Rajak, D. D. P., Pradeep L. Menezes, Emanoil Linul (2019). "Fiber-Reinforced Polymer Composites: Manufacturing, Properties, and Applications." Polymers 11(10): 19-23.

[2] Sharun Hedge, B. S. S., K.N. Chethan (2019). "Review on carbon fiber reinforced polymer (CFRP) and their mechanical performance." materialstoday 19: Pages 658-662.

[3] Andrew Y. Chen, S. B., Austin Turner, Zilan Zhang, Grace X. Gu (2021). "Carbon-fiber reinforced polymer composites: A comparison of manufacturing methods on mechanical properties." International Journal of Lightweight Materials and Manufacture 4(4): 468-479.

[4] S. F. Abdulqadir, B. H. A., and J. O. Sameer (2024). "Comparison of the Mechanical Properties and Approach to Numerical Modeling of Fiber-reinforced Composite, High-Strength Steel and Aluminum." J. Eng. Technol. Sci 56(1): 110–124.

[5] Vlasova, V. (2019). "Using composite materials in aircraft." XLIII ACADEMIC SPACE CONFERENCE 2171(1).

[6] Savage, G. V. (2008). "Composite Materials Technology in Formula 1 Motor Racing." 1-31.

[7] Ruizhen Yang, Y. H., Hong Zhang (2016). "Progress and trends in nondestructive testing and evaluation for wind turbine composite blade." Rewnewable and Sustainable Energy Reviews 60: 1225-1250.

[8] M.-S. Scholz, J. P. B., L.D. Bloom, B.H. Coburn, M. Elkington, J.D. Fuller, M.E. Gilbert, S.A. Muflahi, M.F. Pernice, S.I. Rae, J.A. Trevarthen, S.C. White, P.M. Weaver, I.P. Bond (2011). "The use of composite materials in modern orthopaedic medicine and prosthetic devices: A review." Composites Science and Technology 71(16): 1791-1803.

[9] Sung-Youl Bae, Y.-H. K. (2021). "Study on structural design and analysis of 18 ft CFRP leisure boat." International Journal of Modern Physics B 35(14).

[10] Kaufmann, J. (2015). "New Materials for Sports Equipment Made of Anisotropic Fiber-reinforced Plastics with Stiffness Related Coupling Effect." Procedia Engineering 112: 140-145.

[11] Daniel García Puzuelos Ramos, C. S. M., Ester Olmeda Santamaría, Vicente Díaz López (2020). Publication: Carbon Fiber Reinforced Plastics (CFRP) monocoque structure for Formula Student car, Charles III University of Madrid.

[12] Michael Salvatore DiMilia, A. G. K., Thomas John Hlavenka, Yutong Li, Samantha Clay Chermin, Jamie Marie Donahue, Miguel Goulart Almeida, Alex Joseph

Brown, George Akuamoah Asare (2017). MICRO AIRCRAFT DESIGN DBF-2017, Worcester Polytechnic Institute.

[13] Dipen Kumar Rajak, P. H. W., Emanoil Linul (2021). "Manufacturing Technologies of Carbon/Glass Fiber-Reinforced Polymer Composites and Their Properties: A Review." Polymers 13(21): 1-42.

[14] Qing Wang, L. W., Weidong Zhu, Qiang Xu, Yinglin Ke (2017). "Design optimization of molds for autoclave process of composite manufacturing." Journal of Reinforced Plastics and Composites 36(21): 1564-1576.

[15] Paul Bere, C. N., Razvan Udroiu (2020). "Novel Method for the Manufacture of Complex CFRP Parts Using FDM-based Molds." Polymers 12(10).

[16] Marina Andreozzi, I. B., Tommaso Mancia, Michela Simoncini (2024). "Investigation on the mechanical and environmental behaviour of 3D-printed molds for manufacturing of CFRP components." The International Journal of Advanced Manufacturing Technology 135: 4785-4802.

[17] Picard, M., et al. (2020). "Recent advances in additive manufacturing of engineering thermoplastics: challenges and opportunities." RSC Advances 10(59): 36058-36089.

[18] Ferretti, P., et al. (2021). "Molds with Advanced Materials for Carbon Fiber Manufacturing with 3D Printing Technology." Polymers 13(21): 3700.

[19] Kat de Naoum, R. P. (2025). "3D Printing vs. CNC Machining: Differences and Comparison." Retrieved 1/30/25, 2025.

[20] Danilo D'Andrea, G. R., Marcello Raffaele, Filippo Cucinotta, Dario Santonocito (2022). "Damage assessment of different FDM-processed materials adopting Infrared Thermography." frattura ed integrità strutturale 16: 75-90.

[21] Jan-Anders E. Manson, J. C. S. (1989). "Autoclave Processing of PEEK/Carbon Fiber Composites." Journal of Thermoplastic Composite Material 2(1): 34-49.

[22] N. Soto, C. L., P. Mardones, A. Bayo, C. Rozas, S. Castillo, G. Hamilton, L. Pedrero, S. Zuniga-Fernandez, K. Mauco, H. Hakobyan, C. Garcia, M. R. Schreiber, W. Brooks (2020). "Quality control of the CFRP mirror manufacturing process at NPF."

[23] P.G. Benardos, G.-C. V. (2003). "Predicting surface roughness in machining: a review." International Journal of Machine Tools and Manufacture 43(8): 833-844.

[24] Pulla Sammaiah, K. R., N. Praveenadevi and I. Rajasri Reddy (2020). The Influence Of Process Parameters On The Surface Roughness Of The 3d Printed Part In FDM Process. IOP Conference Series: Materials Science and Engineering. 961.

[25] Gersten, H. S. a. K. (2017). Boundary-Layer Theory. Berlin, Germany, Springer.

[26] Walid Chakroun, I. A.-M., and Sami Al-Fahadformat_quoteCITE (2004). "Effect of Surface Roughness on the AerodynamicCharacteristics of a Symmetrical Airfoil." Wind Engineering 28(5): 547–564.

[27] Alsoufi, M. S. and A. E. E. (2017). "How Surface Roughness Performance of Printed Parts Manufactured by Desktop FDM 3D Printer with PLA+ is Influenced by Measuring Direction." American Journal of Mechanical Engineering 5(5): 211-222.

[28] Irene Buj-Corral, A. D.-F., Ramon Duran-Llucia (2019). "Influence of Print Orientation on Surface Roughness in Fused Deposition Modeling (FDM) Processes." Materials 12(23).

[29] Jasgurpreet Singh Chohan, R. S. (2017). "Pre and post processing techniques to improve surface characteristics of FDM parts: a state of art review and future applications." Rapid Prototyping Journal 23(3).

[30] J. Martinez, J. L. D., A. Pereira, J.A. Pérez (2012). Modelization of surface roughness in FDM parts. MANUFACTURING ENGINEERING SOCIETY INTERNATIONAL CONFERENCE: 849–856

[31] M. Ehsanul Haque, D. B., Swayam Bikash Mishra, Basanta Kumar Nanda (2019). "A Numerical Approach to Measure the Surface Roughness of FDM Build Part." Materials Today: Proceedings 18: 5523-5529.

[32] Pulla Sammaiah, K. R., N. Praveenadevi and I. Rajasri Reddy (2020). The Influence Of Process Parameters On The Surface Roughness Of The 3d Printed Part In FDM Process. IOP Conference Series: Materials Science and Engineering, Purpose-Led Publishing. 981.

[33] Radomir Mendricky, D. F. (2020). "Analysis of the Accuracy and the Surface Roughness of FDM/FFF Technology and Optimisation of Process Parameters." 27(4).

[34] Çağın Bolat, B. E. (2022). "An Investigation on Dimensional Accuracy of 3D Printed PLA, PET-G and ABS Samples with Different Layer Heights." Cukurova University Journal of the Faculty of Engineering 37(2): 449-458.

[35] Bin Li, J. Y., Hai Gu, Jie Jiang, Jie Zhang and Jianhua Sun (2021). "Surface roughness of PLA parts by FDM with chemical treatment." Journal of Physics: Conference Series.

[36] Raluca Maier, S.-G. B., Andrei Christian Mandoc (2022). "Reducing Surface Roughness of 3D Printed Short-Carbon Fiber Reinforced Composites." Materials(16).

[37] Tao Bai, J. L., Weihao Zhang, Zhengping Zou (2014). "Effect of surface roughness on the aerodynamic performance of turbine blade cascade." Propulsion and Power Research.

[38] (2025). "Ender 3 V2 3D Printer." Retrieved 2-25-25, 2025, from https://www.creality.com/products/ender-3-v2-3d-printer-csco.

[39] (2025). "Overture PLA." Retrieved 2-26-25, 2025, from https://overture3d.com/collections/3dprinting-pla-collection/overture3d/products/overturepla.

[40] (2025). "Overture ABS 3D Printer Filament 1.75mm." Retrieved 2-26-25, 2025, from https://overture3d.com/products/overture-abs-filament-1-75mm.

[41] (2025). "Overture PETG 3D Printer Filament 1.75mm." Retrieved 2-26-25, 2025, from https://overture3d.com/products/petg-3dprintingfilament.

[42] (2025). "Filament Properties Table." Retrieved 2-26-25, 2025, from https://www.simplify3d.com/resources/materials-guide/properties-table/.

[43] Miller, S. (2019). Evaluation of Temperature Gradients During Cure of a Thick Carbon Fiber/Epoxy Composite. Cleveland, OH, NASA Glenn Research Center.

[44] Boissonneault, T. (2024). "PLA and Acetone? Here are Better Ways to Smooth PLA 3D Prints." Retrieved 2-26-25, 2025, from https://www.wevolver.com/article/acetone-pla

[45] O'Neill, B. (2024). "ABS Smoothing: Acetone Vapor Baths & Other Ways to Remove Layer Lines." from https://www.wevolver.com/article/petg-adhesion?

[46] Moody, J. (2024). "PETG Smoothing: 5 Ways to Smooth PETG." Retrieved 2-26-25, 2025, from https://all3dp.com/2/petg-smoothing/.

[47] . "NACA 2412 (naca2412-il)." Retrieved 3-1-25, 2025, from http://airfoiltools.com/airfoil/details?airfoil=naca2412-il.

[48] Haberkorn, T. (2016). Aircraft separation in uncontrolled airspace including human factors, Graz University of Technology.

[49] Muhammad Robby, A. K., Refdinal, Yolli Fernanda (2024). "Aerodynamic Analysis of NACA 2412 Airfoil on UAVAircraft Wing Using Ansys Fluent Software " International Journal of Innovation in Mechanical Construction and Energy 1(3): 156–165.

[50] Benoit Pernet, J. K. N., Hao Zhang (2022). "Compressive Strength Assessment of 3D Printing Infill Patterns." Procedia CIRP 105: 682-687.

[51] (2020). "Modix Large Scale 3D Printers." Retrieved 3-2-25, 2025, from https://www.modix3d.com/.

[52] (2025). "bigrep one." Retrieved 3-2-2025, 2025, from https://bigrep.com/bigrep-one/.

[53] Casabar, J. (2025). "Layer Height." Retrieved 3-4-25, 2025, from https://buildit.sdsu.edu/layer-height/.

[54] (2025). "Carbon Fiber Fabric 2×2 Twill 3k 50″/127cm 6oz/203gsm Hexcel AS4." Retrieved 3-4-25, 2025, from https://compositeenvisions.com/product/carbon-fiber-fabric-2x2-twill-3k-50-127cm-6oz-203gsm-hexcel-as4/.

[55] (2025). "Thin Epoxy Resin." Retrieved 3-5-25, 2025, from https://compositeenvisions.com/product/thin-epoxy-resin/.

[56] (2025). "3:1 Epoxy Hardener – Medium Cure." Retrieved 3-6-25, 2025, from https://compositeenvisions.com/product/31-epoxy-hardener-medium-cure-1161/.

[57] (2022). "Resin to Fiber Ratio Explained." Retrieved 3-6-26, 2025, from https://compositeenvisions.com/document/resin-to-fiber-ratio-explained/#:~:text=Accounting%20for%20a%20rough%20estimate,and%20ensure%20underestimating%20is%20eliminated.&text=Using%20a%204%3A1%20fast,a%20quart%20of%20mixed%20resin.

[58] (2025). "GOYOJO Surface Roughness Tester - 0.001μm." Retrieved 3-6-25, 2025, from https://goyojotools.com/products/goyojo-surface-roughness-tester-0-001%CE%BCm.

[59] (2020). "CFD computational domain." Retrieved 3-10-25, 2025, from https://www.idealsimulations.com/resources/cfd-computational-domain/.

[60] Falk Goetten, D. F. F., Matthew Marino, Cees Bil (2019). A review of guidelines and best practices for subsonic aerodynamic simulations using RANS CFD Asia Pacific International Symposium on Aerospace Technology.

[61] I. H. Abbott and A. E. Von Doenhoff, Theory of Wing Sections: Including a Summary of Airfoil Data. Mineola, NY: Dover Publications, 1959.

[62] Thomas Adams, C. G. (2012). "A Simple Algorithm to Relate Measured Surface Roughness to Equivalent Sand-grain Roughness." International Journal of Mechanical Engineering and Mechatronics 1(1).